2019

Frazil ice growth and ice production during katabatic wind events in Ross Sea polynyas, Antarctica

Lisa Marie De Pace
University of Rhode Island, lisamdepace@gmail.com

FRAZIL ICE GROWTH AND ICE PRODUCTION DURING KATABATIC WIND EVENTS IN ROSS SEA POLYNYAS, ANTARCTICA

BY

LISA MARIE DE PACE

A THESIS SUBMITTED IN PARTIAL FULFILLMENT OF THE

REQUIREMENTS FOR THE DEGREE OF

MASTER OF SCIENCE

IN

PHYSICAL OCEANOGRAPHY

UNIVERSITY OF RHODE ISLAND

2019

MASTER OF SCIENCE THESIS

OF

LISA MARIE DE PACE

APPROVED:

Thesis Committee:

Major Professor Brice Loose

Jaime Palter

Angelo Lucia

Nasser H. Zawia
DEAN OF THE GRADUATE SCHOOL

UNIVERSITY OF RHODE ISLAND
2019

ABSTRACT

During katabatic wind events in the Terra Nova Bay and Ross Sea polynyas, wind speeds exceeded 20 m s^{-1}, air temperatures were below -25 °C, and the mixed layer extended as deep as 600 meters. Yet, temperature and salinity profiles were not perfectly vertical, as one would expect with vigorous convective heat loss. Instead, the profiles revealed bulges of warm and salty water starting at the ocean surface and extending to the top tens of meters. Considering both the colder air above and colder water below, we surmise that the increase in temperature and salinity reflects latent heat and salt release during unconsolidated frazil ice production throughout the upper water column. We use a simplified salt budget to analyze these anomalies to estimate in-situ frazil ice content 5.8 and 0.13 kg within the top 50 m of the water column. Estimates of vertical mixing by turbulent kinetic energy dissipation reveals rapid convection in these unstable density profiles, and mixing lifetimes from 2 to 30 minutes. The corresponding ice production rates yield an average ice thickness of 52 cm day^{-1}, which compares well with previous empirical and model estimates. However, our individual estimates of production up to 358 cm day^{-1} reveal the intensity of short-term ice production in the windiest sections of the Terra Nova Bay Polynya.

ACKNOWLEDGMENTS

I would like to thank Dr. Brice Loose for support through this thesis and my time at the Graduate School of Oceanography. He supported me through the research process and encouraged me to always ask one more question. I would also like to thank my committee of Dr. Jaime Palter and Dr. Angelo Lucia for their time. I would like to thank the Graduate School of Oceanography for their support.

I appreciate the support of the University of Wisconsin-Madison Automatic Weather Station Program for the data set, data display, and information, NSF grant number ANT-1543305.

PREFACE

This Master of Science Thesis is in Manuscript format.

TABLE OF CONTENTS

LIST OF TABLES

LIST OF FIGURES

FIGURE PAGE

MANUSCRIPT

Frazil Ice growth and ice production during katabatic wind events in Ross Sea polynyas, Antarctica has been prepared for submission in:

Journal: The Journal of Glaciology

Status: Coauthor Review

List of Coauthors:

Brice Loose- University of Rhode Island

Madison Smith- University of Washington

Sharon Stammerjohn- University of Boulder, Colorado

Jim Thomson- University of Washington

Steve Ackley- University of Texas

1. INTRODUCTION

Latent heat polynyas form in areas where prevailing winds or oceanic currents create divergence in the ice cover, leading to openings surrounded by extensive pack ice (Armstrong, 1972; Park et al, 2018). The open water of polynyas is critical for air-sea-heat-exchange, since ice covered waters are better insulated (Talley et al, 2011). Figure 1 provides a schematic of a coastal latent heat polynyas. Katabatic winds cold, dense air masses that form over the continental ice sheets of Antarctica flow as sinking gravity currents, that descend off the glaciated continent and in the case of the Ross Sea, off the Transantarctic mountain ranges. These flows are often funneled and strengthened by mountain-valley topography. The katabatic winds create and maintain latent heat polynyas. This research focuses on results from two coastal latent heat polynyas in the Ross Sea, which will be referred to simply as polynyas moving forward.

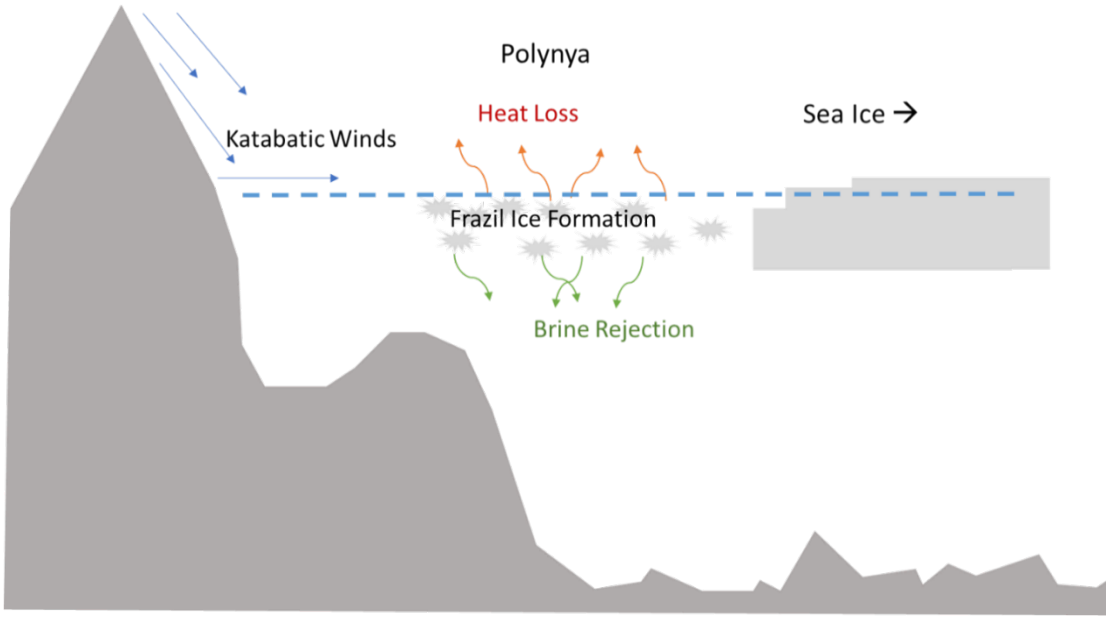

Figure 1: Schematic of a latent heat or coastal polynya. The polynya is kept open from katabatic winds which drive ice advection, oceanic heat loss and frazil ice formation. Ice formation results in oceanic loss of latent heat to the atmosphere and brine rejection (Talley et al, 2011).

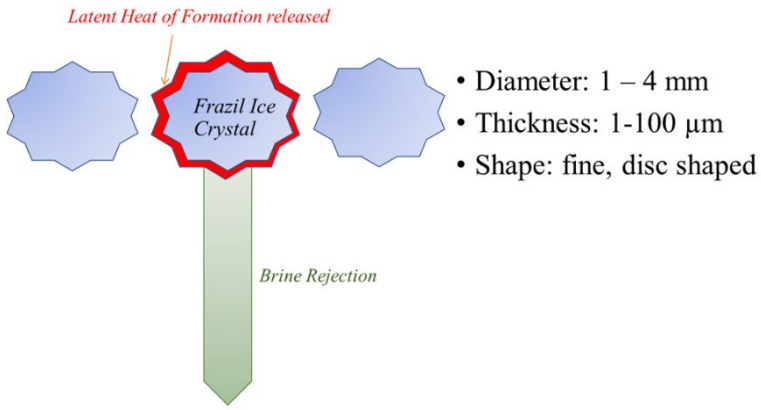

Figure 2: Schematic of Frazil Ice formation. Adapted from (Ushio and Wakatsuchi, 1993) this figure depicts the release of latent heat of fusion and brine rejection as a frazil ice crystal is formed. Includes key features of frazil ice crystals including diameter, thickness, and shape.

Polynyas drive extreme oceanic heat loss which creates in-situ "supercooled" water, that is colder than the freezing point (Skogseth et al, 2009). Two criteria for ice production in polynyas from supercooled water are large net heat loss from the water and transport of the frazil ice away from the formation region; both criteria are achieved in the polynya by katabatic winds and cold air temperatures (Coachman, 1966). These conditions generate sea ice as fine disc-shaped or dendritic crystals called frazil ice. These frazil ice crystals depicted in Figure 2, measure about 1-4 millimeters in diameter and 1-100 micrometers in thickness (Ushio and Wakatsuchi, 1993). Katabatic winds sustain the polynya by clearing frazil ice, forming pancake ice which piles up at the polynya edge to form a consolidated ice cover (Morales Maqueda et al, 2004). The production and sweeping away of frazil ice crystals creates an-efficient ice production mechanism whereby seawater is kept in contact with cold air, unmitigated by an insulating layer of ice (Ushio and Wakatsuchi, 1993).

Brine rejection (Cox and Weeks, 1983) and a large amount of latent heat release accompany the continuous ice production. In the Ross Sea, these coastal polynyas produce the precursor to Antarctic Bottom Water, a water mass known as High Salinity Shelf Water (HSSW) that is created by the large volumes of brine rejection (Martin et al, 2007; Sansivero et al, 2017; Tamura et al, 2007; Jacobs, 2004; Petrelli et al, 2008; Cosimo & Gordon, 1998; Kurtz & Bromwich, 1985).

Given the importance of Antarctic Bottom Water to global circulation, polynya ice production rates have been widely studied and modeled. Gallee (1997), Petrelli et al (2008), Fusco et al (2002), and Sansivero et al (2017) used models to calculate polynya production rates on the order of tens of centimeters per day. Schick et al (2018) and Kurtz and Bromwich (1985) used heat fluxes to estimate polynya ice production rates, also on the order of tens of centimeters of ice thickness per day. However, quantitative estimation of polynya ice production is challenging due to the difficulty of obtaining in-situ measurements (Tamura et al, 2007).

During a late autumn 2017 oceanographic cruise expedition to the Ross Sea as part of the PIPERS (Polynyas, Ice Production and seasonal Evolution in the Ross Sea) project, Conductivity, Temperature, and Depth (CTD) vertical profiles acquired in the Ross Sea coastal polynyas indicated anomalous regions of saltier, warmer water near the surface. Simultaneously, visual field observations noted active frazil ice formation in these same locations. We hypothesize that the excess temperature is evidence of latent heat of fusion from frazil ice formation and that the excess salinity is evidence of brine rejection from frazil ice formation. We evaluate the reliability of these CTD measurements by comparing the shape and size of the profile anomalies with estimates

of the CTD precision and stability, and by using supporting evidence of the atmospheric conditions that are thought to drive frazil ice formation (e.g. temperature and wind speed). Next, we estimate the production of frazil ice using the temperature and salinity anomalies. Finally, we attempt to put bounds on the mixing timescale of these anomalies, by asking how long they would take to mix into the background, if the formation process ceased. This, in turn provides an estimate of near instantaneous frazil ice production. Last, we discuss the implications of these results.

2. STUDY AREA AND DATA

2.1 The Terra Nova Bay Polynya and Ross Sea Polynya

The Ross Sea, a southern extension of the Pacific Ocean, abuts Antarctica along the Transantarctic Mountains and has three recurring latent heat polynyas: Ross Sea polynya (RSP), Terra Nova Bay polynya (TNBP), and McMurdo Sound polynya (MSP) (Martin et al, 2007). The RSP is Antarctica's largest recurring polynya; it forms in the central and western Ross Sea (Park et al, 2018). The average area of the RSP is 27,000 km^2 but can grow as large as 50,000 km^2, depending on environmental conditions (Park et al, 2018; Morales Maqueda et al, 2004). It is located to the east of Ross Island, adjacent to the Ross Ice Shelf, and typically extends the entire length of the Ross Ice Shelf (Martin et al, 2007; Morales Maqueda et al, 2004). TNBP, located to the north of Drygalski ice tongue, and MSP, the smallest of the three polynyas, are both located in the western Ross Sea, depicted in Figure 3 (Petrelli et al, 2008). The area of TNBP, on average is 1000 km^2, but can extend up to 5000 km^2; the oscillation period is 15-20 days (Morales Maqueda et al, 2004). This paper focuses primarily on TNBP and secondarily on RSP.

During the autumn and winter season, Morales Maqueda et. al (2004) estimated TNBP cumulative ice production around 40-60 meters of ice, or approximately 10% of the annual sea ice production that occurs on the Ross Sea continental shelf. The RSP, while having a lower daily ice production rate, produces three to six times as much as TNBP annually due to its much larger size (Petrelli et al, 2008). Ice production in polynyas plays an important role in the modification of HSSW. In areas over the continental shelf, brine rejection paired with super-cooled temperatures at or below the freezing point produces especially dense shelf waters (Talley et al, 2011). In the case of the Ross Sea, the cold, dense HSSW formed on the shelf eventually becomes Antarctic Bottom Water off the shelf, the densest water in global circulation. TNBP produces especially dense HSSW, driven by its higher salinity, and despite being smaller than RSP, it produces approximately 1-1.23 Sv annually (Buffoni et al, 2002; Fusco et al, 2009; Orsi & Wiederwohl, 2009; Kurtz & Bromwich 1985, Van Woert 1999b).

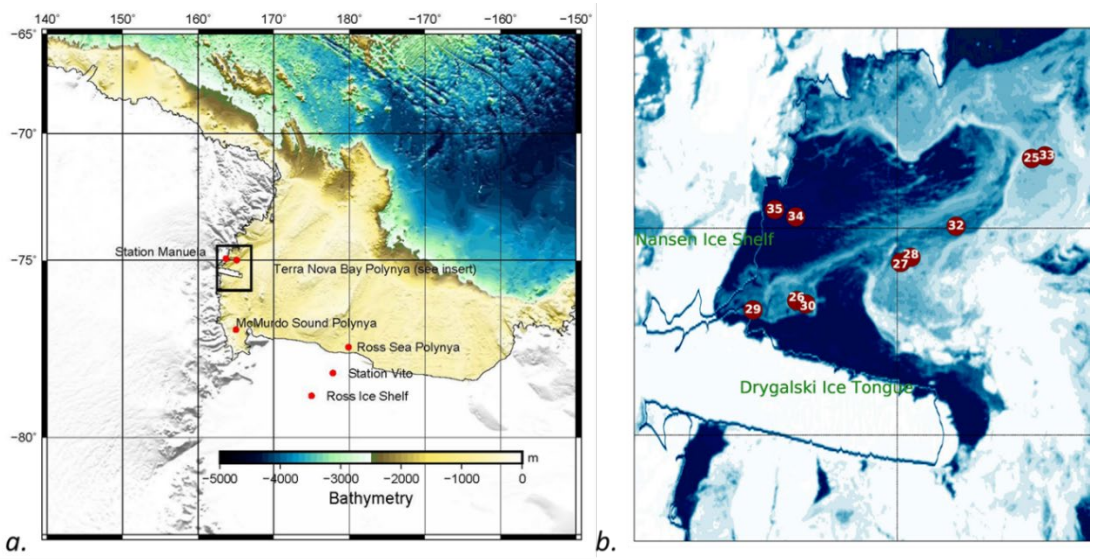

Figure 3: Map of the Ross Sea and Terra Nova Bay Polynya. a) Overview of the Ross Sea, Antarctica highlighting the locations of the three recurring polynyas: Ross Sea Polynya (RSP), Terra Nova Bay Polynya (TNBP), and McMurdo Sound Polynya (MSP). Map highlights the 2014 General Bathymetric Chart of the Oceans one-degree grid. Color bar selected to highlight bathymetry changes around 2500 meters. b) Terra Nova Bay Polynya Insert as indicated by black box in panel a. MODIS image of TNBP with the 10 CTD stations with anomalies shown. Not included is CTD Station 40, the one station with an anomaly located in the RSP. Date of MODIS image March 13, 2017; date was selected, despite being outside research dates due to available light for image and low cloud clover.

2.2 PIPERS Expedition

We collected our data during the 63-day PIPERS expedition aboard the RVIB Nathaniel B. Palmer (NB Palmer, NBP17-04). More information about the research activities during the PIPERS expedition are available at http://www.utsa.edu/signl/pipers/index.html. The Expedition was a late autumn cruise, spanned from April 11 to June 14, 2017. Vertical profiles of Conductivity, Temperature, and Depth (CTD) were taken at 58 stations within the Ross Sea. For the purposes of this study, we focus on the 13 stations (CTD 23-35) that occurred within the TNBP and 4 stations (CTD 37-40) within the RSP during katabatic wind events.

2.3 The Seabird 911 CTD

The CTD profiles were carried out using a Seabird 911 CTD (SBE 911) attached to a 24 bottle CTD rosette, which is supported and maintained by the Antarctic Support Contractor (ASC). The SBE 911 was deployed from the starboard Baltic Room. The reported initial accuracy for the SBE 911 is ± 0.0003 Siemens meter^{-1} (Sm^{-1}), ± 0.001 ℃, and 0.015% of the full-scale range of pressure for conductivity, temperature, and depth respectively. Independent of the accuracy stated above, the SBE 911 can resolve differences in conductivity, temperature, and pressure on the order of 0.00004 S/m, 0.0002 ℃ and 0.001% of the full range, respectively (SeaBird Scientific, 2018). The instrument resolution is an important parameter for this research, because the anomalous profiles were identified by comparing the near surface CTD measurements with other values within the same profile in order to report the thermal and haline anomalies. The SBE 911 samples at 24 Hz with an e-folding time response of 0.05 seconds for conductivity and temperature. The time response for pressure is 0.015 seconds. Each cast contains both a down cast profile and up cast profile. The down and up casts were separated using the maximum depth as an index. In many instances, the up cast recorded a similar thermal and haline anomaly, however the 24 bottle CTD rosette package creates a large wake that disturbs the readings on the up cast. Therefore, we use only the down cast profiles for this analysis.

The SBE 911 data were post-processed with post-calibrations by Seabird, following standard protocol, and quality control parameters. Profiles were bin-averaged at two size intervals: one-meter depth bins and 0.1-meter depth bins, to compare whether bin averaging influenced the heat and salt budgets. We observed no

difference between the budget calculations derived from one-meter vs 0.1-meter bins; the one-meter bins are presented in this publication. All thermodynamic properties of seawater were evaluated via the Gibbs Seawater toolbox which uses the International Thermodynamic Equation of Seawater – 2010 (TEOS-10).

2.4 Weather observations

During the PIPERS expedition, multiple katabatic wind events were observed within the TNBP and RSP. The NB Palmer was in TNB from May 1 through May 13; during this period the hourly wind speed and air temperature data from Weather Station Manuela, shown on Figure 3a, the automatic weather station on Inexpressible Island, was compared to NB Palmer's meteorological suite, normalized to a height of 10 meters, Figure 4. In most cases, the winds and air temperature from both locations follow the same pattern, with shipboard observations from the NB Palmer observations being lower in intensity (lower wind speed, warmer temperatures) than Station Manuela. While in the RSP May 16-18, the wind speed and air temperature from NB Palmer is compared to Station Vito, shown on Figure 3a and located on the Ross Shelf Ice Sheet. At Station Vito, the air temperature is colder, but the wind speed is less intense, most likely due to higher drag across the ice sheet.

During the CTD sampling within TNBP there were 4 periods of intense katabatic winds, with each period lasting for 24 hours or longer. During the CTD sampling within RSP there was one period of near katabatic strength winds that lasted 24 hours or longer. During each wind event, the air temperature oscillated in a similar pattern and ranged from approximately -10 ℃ to -30 ℃.

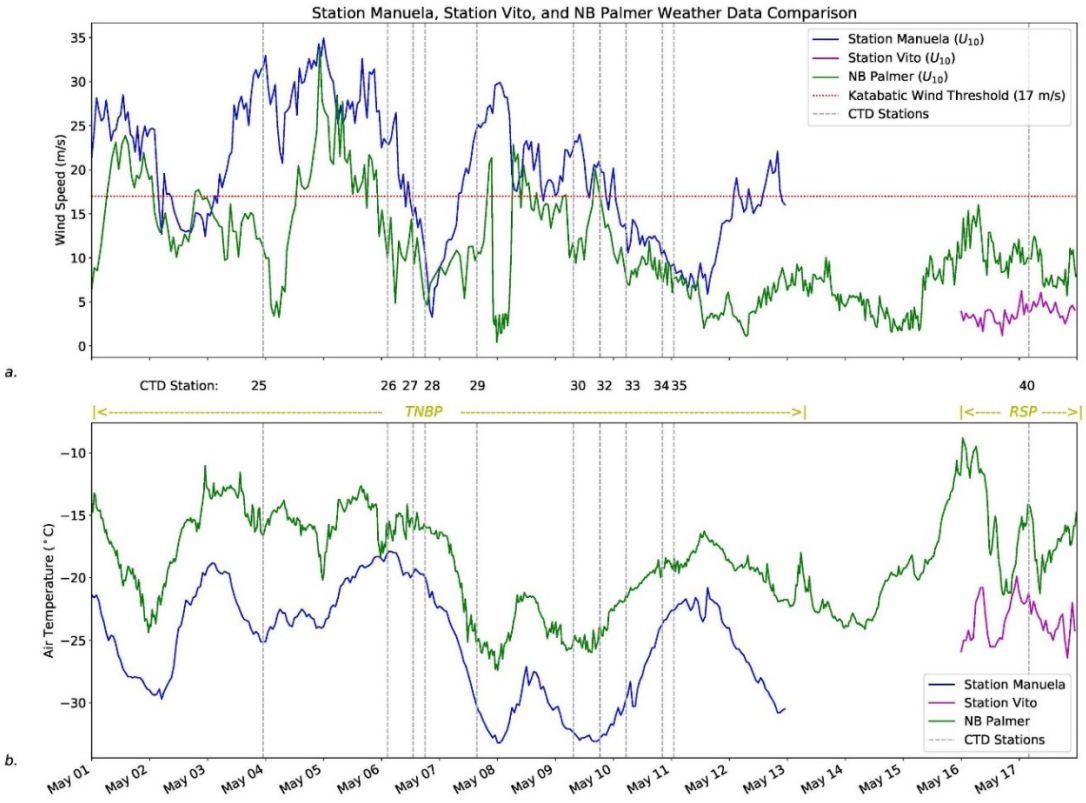

Figure 4: Wind speed and air temperature from 01 May to 17 May 2017. a.) Wind speed from Station Manuela, Station Vito, and NB Palmer from 10 meters. The commonly used katabatic threshold of 17 $ms^{-1}$is depicted as a "dotted red line", as well as the date and start time of each CTD cast. b) Air temperature from both Station Manuela, Station Vito, and NB Palmer.

3. EVIDENCE OF FRAZIL ICE FORMATION

During PIPERS, the CTD profiles acquired in the RSP and TNBP defied expectations for vertical profiles in the presence of strong winds. Despite air temperatures well below freezing and strong winds, the profiles presented with anomalous regions of warmer water near the surface. The excess temperature was accompanied by anomalous regions of saltier water. Simultaneously, visual field observations noted active frazil ice formation in these same locations. We suggest that the excess temperature is evidence of latent heat of fusion from frazil ice formation and that the excess salinity is evidence of brine rejection from frazil ice formation.

We evaluate the reliability of these CTD measurements by comparing the shape and size of the profile anomalies with estimates of the CTD accuracy, and by using supporting evidence of the atmospheric conditions that are thought to drive frazil ice formation (e.g. temperature and wind speed). Next, we estimate the production of frazil ice using the temperature and salinity anomalies.

3.1 Selection of profiles of interest

We used the following selection criteria to identify profiles from the two polynyas that appeared to be under the influence of frazil ice formation: (1) a deep mixed layer extending several hundred meters, and down to 600 meters in one case (Figure 5) (2) in-situ temperature readings falling below the freezing point in the near-surface water, (3) an anomalous bulge of warm water within the top 20 meters of the profile (Figure 6), and/or (4) an anomalous bulge of salty water within the top 20 meters of the profile (e.g. Figure 7). Each temperature profile was individually plotted over the entire depth range to identify the deep mixed layer, ranging from 100 to 600 meters.

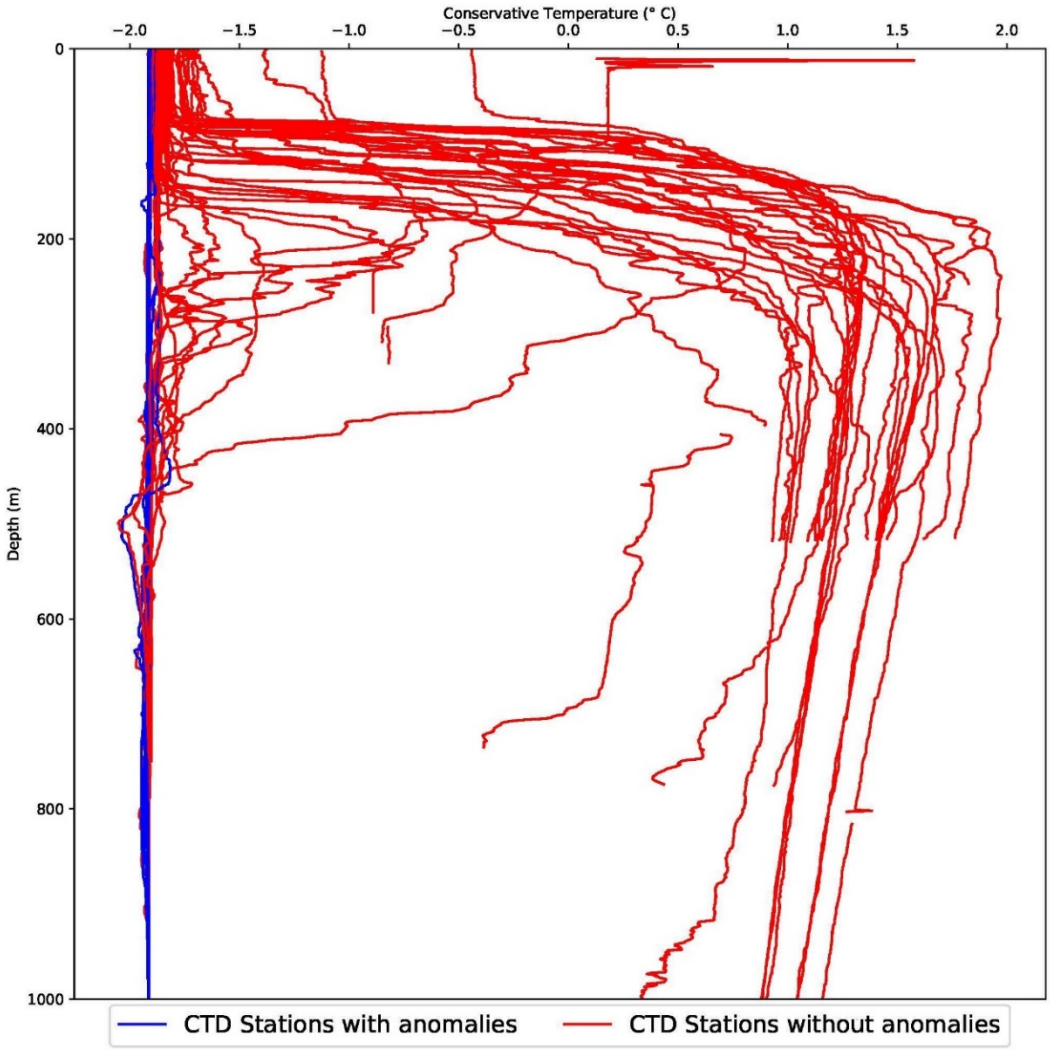

Figure 5: 1000-meter Conservative Temperature profiles of all 57 out of 58 PIPERS CTD stations. One station not included due to significantly warmer temperature outside temperature range shown here. The CTD stations from TNB and RS with frazil ice anomalies and deep mixed layers are highlighted in blue and the stations without anomalies are represented in red. In addition to the large mixed layer, these profiles also represent the coldest temperatures.

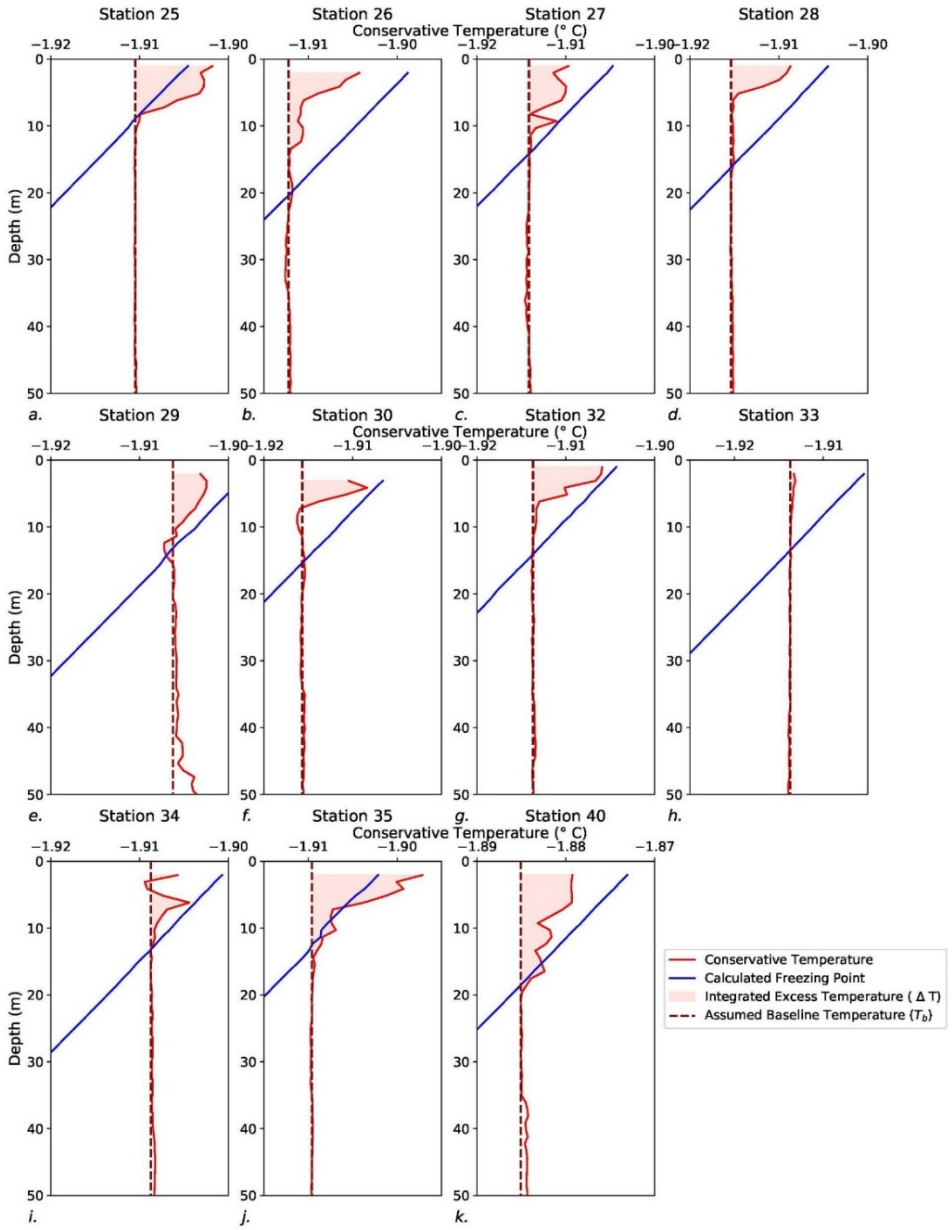

Figure 6: Conservative Temperature profiles from CTD down casts from all 11 stations with anomalies and depicting the supercooled water at the surface and the anomalous temperature bulge. All of the plots (a- h) have an x-axis representing 0.02 ∘ C. a-j) TNBP, k) RSP

The temperature profiles were examined by plotted over only the top 50 meters of the water column, as in Figure 6, to evaluate criteria 2 and 3. In these plots, we observe excess temperature anomalies over the top 10-20 m, and near-surface temperature close to the freezing point were identified at nine TNBP stations and one RSP station. The excess salinity anomalies, shown in Figure 7, were also observed at the stations showing excess temperature anomalies, with two exceptions: Station 26 has a measurable temperature anomaly (Figure 6b) and no a discernible salinity anomaly (Figure 7b), and Station 33 has a measurable salinity anomaly (Figure 7h) but not a discernible temperature anomaly (Figure gh). The stations of interest are listed in Table 1.

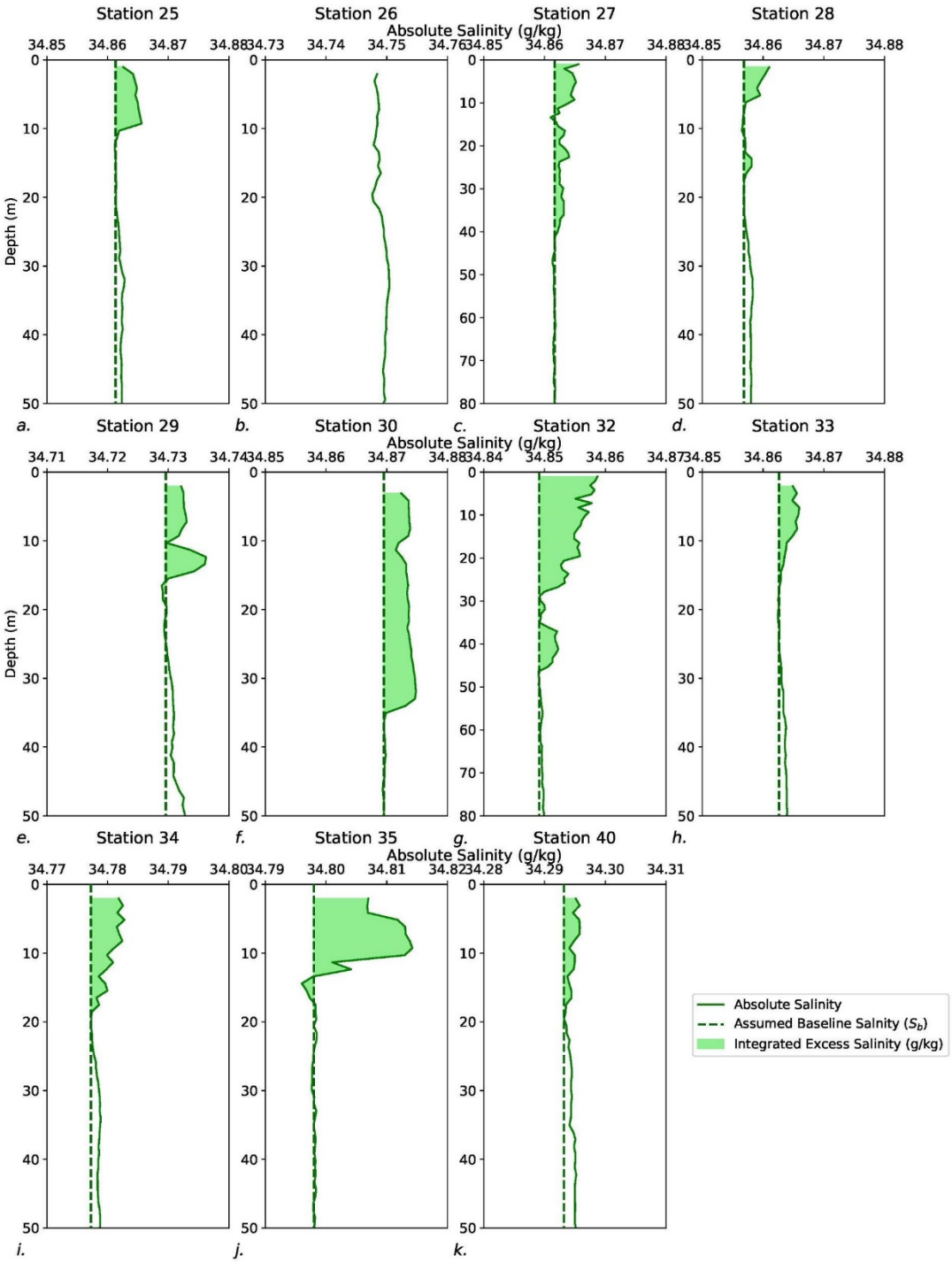

Figure 7: Absolute Salinity profiles from CTD down casts at all 11 stations depicting the anomalous saline bulge in the top 10-20 meters. Figure 7.b and 7.e have a salinity anomaly that approaches 50 meters, so the plot extends to 80 meters to best highlight it. All of the plots (a- h) have an x-axis representing 0.03 g kg^{-1}.

3.2 Evaluating the fidelity of the CTD measurements

To evaluate the uncertainty associated with the temperature and salinity anomalies at each of the polynya stations, we compared each anomaly to the initial accuracy of the SBE 911: ± 0.001 ℃ and ± 0.0003 S m^{-1} or 0.00170 g kg^{-1} when converted to absolute salinity. To quantify the maximum amount of the temperature anomaly, the baseline excursion, ΔT, was calculated throughout the anomaly $\Delta T = T_{obs} - T_b$, where T_{obs} is the in-situ conservative temperature and T_b is the in-situ baseline, which is extrapolated from the far field conservative temperature within the well-mixed layer below the anomaly. Taking the single largest baseline excursion from each of the 11 anomalous CTD profiles and averaging them, we compute the average baseline excursion of 0.0064 ◦C. While, this is a small change in the temperature, it is still 32 times larger than the stated precision of the SBE 911 (0.0002 ℃). The same approach applied to the salinity anomalies is 0.0058 g kg^{-1}, which is 10 times larger than the instrument precision (0.00004 S m^{-1}). Table 1 includes the maximum temperature and salinity anomalies for each CTD station.

One concern was that frazil ice crystals could interfere with the conductivity sensor. It is possible that ice crystals smaller than 5 mm can be ingested into the conductivity cell and create spikes in the raw conductance data. Frazil crystals smaller than 100 μm are theoretically small enough to fit in between the conductivity cell electrodes and thereby decrease the conductance/salinity that is reported by the instrument (Skogseth & Smedsrud, 2009). To test for frazil interference, the absolute salinity was plotted from raw conductivity data and from 1-meter binned data for the CTD Stations with anomalies, Supplemental Figure 1.The raw data shows varying

levels of noise in the signal and spikes of lesser magnitude values that are likely due to frazil ice crystal interference. However, the 1-meter binned data, does not follow the spike excursions, indicating that binning minimizes or removes the effects of the noise and spikes. We conclude that there is frazil interference in the conductivity, but the lesser magnitude and 1-meter bins negates the effects.

Considering the consistency of the temperature and salinity measurements within and below the anomalies, and also considering the repeated observation of anomalies at 11 CTD stations, we infer that the observed anomalies are not an instrumental aberration and can be interpreted as valid CTD profiles.

3.3 EISCam Observations of frazil ice formation

During PIPERS a EISCam (Evaluative Imagery Support Camera) version 2 instrument was operating in time lapse mode, recording figures of the ocean surface continuously. The images of the water surface, that coincide in time with the 11 anomalous CTD profiles, reveal long streaks and large aggregations of frazil ice in every frame (Figure 8). The winds were strong enough at all times to set up wave fields or advect frazil ice and resulted in downstream frazil streaks and pancake ice in most situations. Smaller frazil streaks and a curtain of frazil ice below the frazil streak are also visible.

Figure 8: Images from NB Palmer as EISCam (Evaluative Imagery Support Camera) version 2. White areas in the water are loosely consolidate frazil ice crystals being actively formed during a katabatic wind events. d.) brightened to allow for better resolution.

3.4 Parallels between the PIPERS profiles and lab experiments

Ushio and Wakatsuchi (1993) conducted laboratory experiments to reproduce the conditions observed in polynyas. They exposed their tank, measuring 2-m length, 0.4-m width and 0.6-m depth to air temperatures at -10 ℃ and wind speeds of $6m\ s^{-1}$. They observed supercooling in the range of 0.1 to 0.2 ℃ at the water surface and found that after 20 minutes the rate of super-cooling slowed due to release of latent heat, coinciding with visually observed frazil ice formation. Simultaneously with formation of frazil ice crystals, they observed an increase in salinity from the rejection of brine. After ten minutes of ice formation, the temperature of the frazil ice layer was 0.07 ℃ warmer and the layer was 0.5 to 1.0% saltier (Ushio and Wakatsuchi, 1993).

In this study, we found the frazil ice layer to be on average 0.0064 ℃ warmer than the underlying water. Similarly, the salinity anomaly was on average 0.0058 g kg^{-1} saltier, which equates to 0.017% saltier than the water below. While our anomalies were significantly smaller than those observed in this experiment, the same trend of super-cooling, followed by onset of frazil ice formation and the appearance of a salinity anomaly, was observed during PIPERS as by Ushio and Wakatsuchi (1993). The forcing conditions and dimension constraints of the tank experiment can explain the discrepancies in the size of temperature and salinity anomalies formed.

3.5 Similarities to Platelet Ice formation

In the polynya, katabatic winds and sub-freezing air temperatures create supercooled water near the surface, which in turn drives frazil ice formation. While the mechanism for supercooling differs, Robinson et al (2017) investigated ice formation under the McMurdo Sound Ice Shelf. As Ice Shelf Water Plumes (ISW) approached the ice surface, the pressure change leads to the formation of supercooled water and frazil ice formation. As the frazil crystals continue to grow, they maintain their geometry and form platelet ice. In the depth range of ice formation, Robinson et al. (2017) found an increase in salinity from brine rejection and an increase in temperature from latent heat release during ice formation. These vertical trends in temperature and salinity are similar to our results.

3.6. The anomalous profiles from TNBP an RSP appear to trace active frazil ice formation

Throughout sections 2 and 3, we have documented that the anomalous profiles from TNBP and RSP appear to trace frazil ice formation. In §3.1 and §3.2, we showed

that the CTD profiles in both temperature and salinity are reproducible and large enough to be distinguished from the instrumental noise. In §2.4, the strong winds and sub-zero air temperatures supported both ice formation and advection. The coincident EISCam measurements reveal significant accumulation of frazil ice crystals on the ocean surface, while the NB Palmer was in TNBP and RSP. In §3.4 and §3.5, we note the commonalities between the PIPERS polynya profiles and frazil ice formation during platelet ice formation and during laboratory experiments of frazil ice formation. Given the correlation of strong winds, cold air temperatures, water temperature around the freezing point, we find no simpler explanation for the apparent warmer, saltier water near the surface of these 11 CTD profiles. Considering the similarity in conditions found during lab experiments, platelet ice formation, we concluded these profiles reflect measurable frazil ice formation.

4. ESTIMATION OF FRAZIL ICE CONCENTRATION USING CTD PROFILES

Having selected the CTD profiles that reveal frazil ice formation, we next ask "how much frazil ice formation is inferred by these T and S profiles?". The inventories of heat and salt from each profile can provide independent estimates of frazil ice mass, that should be comparable. To simplify the inventory computations, we neglected the horizontal advection and diffusion of heat and salt; this is akin to assuming that lateral variations are not important because the neighboring water parcels are also experiencing the same intense vertical gradients in heat and salt. We first describe the computation using temperature in § 4.1 and the computation using salinity in § 4.2.

4.1 Estimation of frazil ice concentration using temperature anomalies

We used the temperature profiles to compute the "excess" heat inside the anomaly. Utilizing the latent heat of fusion as a proxy for frazil ice production we estimated the amount of frazil ice that would be formed in order to create such an anomaly. For each station, we first estimated the enthalpy inside the temperature anomaly (Talley et al, 2011) as follows. Within each CTD bin, we estimated the excess temperature $\Delta T = T_{obs} - T_b$, where T_{obs} is the in-situ conservative temperature and T_b is the in-situ baseline or far field conservative temperature. The excess over the baseline is graphically represented in Figure 9a. Because we lacked multiple profiles at the same location, we were not able to observe the time evolution of these anomalies. Consequently, T_b represents our best inference of the temperature of the water column prior to the onset of ice formation; it is highlighted in Figure 9a with the dashed line. We established T_b by looking for a near constant value of temperature in the profile directly below the temperature bulge. In most cases the temperature trend over depth was very linear, monotonic and close to the freezing point, however it did have slight variations. After selecting the starting location, the conservative temperature was averaged over 10 meters to remove slight variations in the conservative temperature and minimizing selection bias.

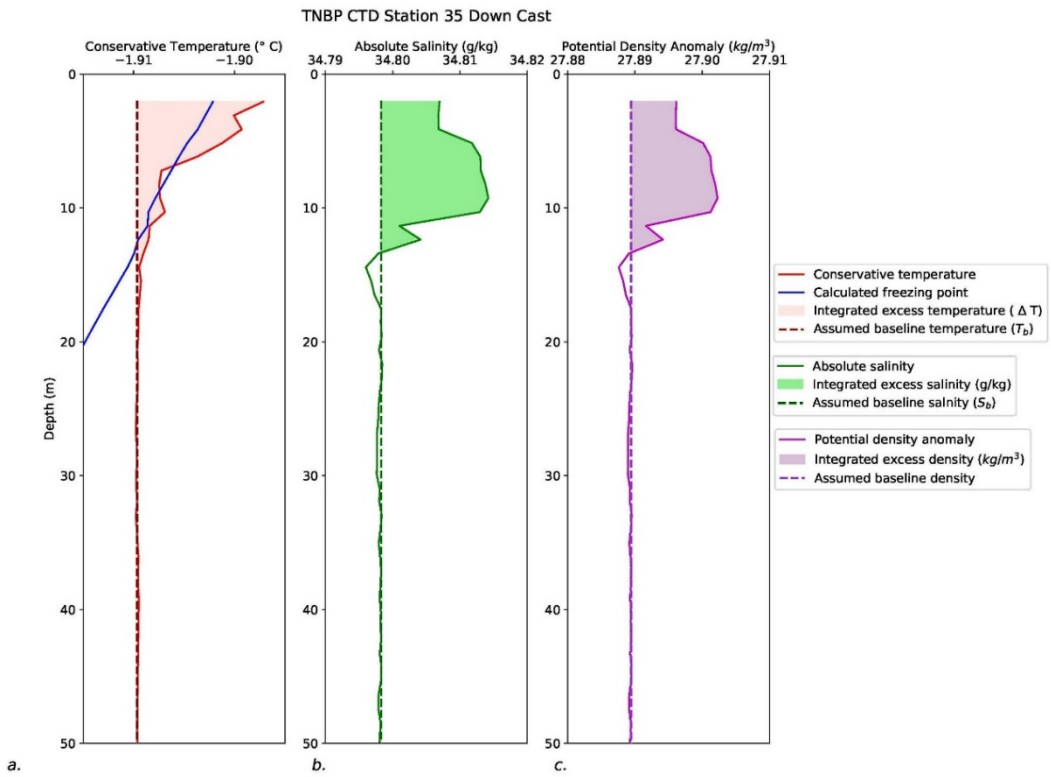

Figure 9: Conservative temperature, absolute salinity, and potential density anomaly for TNBP CTD Station 35, May 10, 2017. a) Conservative temperature profile showing the temperature anomaly, the selected baseline temperature (dashed line) and the integrated excess temperature (shaded area). b) Absolute salinity profile showing the salinity anomaly, the selected baseline salinity (dashed line), and integrated excess salinity (shaded area). c) Potential density anomaly showing the selected baseline density and the excess density instability.

To find the excess heat (Q_{excess}^{total}) represented in the total thermal anomaly, we computed the vertical integral of heat per unit area from the surface (z=0) to the bottom of the anomaly (z=H) :

$$Q_{excess}^{total} = \int_{z=0}^{z=H} \rho \;\; C_p \;\; \Delta T \;\; A \, dz \qquad (1)$$

Here ρ =density of seawater, z= the depth range of the anomaly, C_p= the specific heat capacity, and A= an area of 1 m^2. All thermodynamic properties of seawater were evaluated via the Gibbs Seawater toolbox which uses the International Thermodynamic Equation of Seawater – 2010 (TEOS-10). The mass of frazil ice is

estimated by applying the Latent heat of formation (L_f =330 kJ kg^{-1}) as a conversion factor to Q_{excess}^{total} :

$$Mass_{ice}^{temp} = \frac{Q_{excess}^{total}}{L_f} \quad (2)$$

The Mass of ice derived represents the total mass of ice, in kg, in the volume of water, $V = z * A$. A more detailed explanation of equations 1 and 2 is contained in Supplemental 1. The mass of ice derived from the temperature anomaly for each station is listed in Table 1.

4.2 Estimation of frazil ice concentration using Sea Bird CTD Salinity profiles

The mass of salt within the salinity anomaly was used to estimate ice formation. Assuming that frazil ice crystals do not retain any brine and assuming there is no evaporation, the salinity anomaly is directly proportional to the ice formed. By using the conservation of mass equations for water and salt, the mass of frazil ice can be estimated by comparing the excess salt (measured as salinity) with the amount of salt initially present in the profile. The conservation of mass equations used, and subsequent derivations are included in Supplemental 2. The salinity anomaly (ΔS) above the baseline salinity (S_b) is $\Delta S = S_{obs} - S_b$, and is shown in Figure 9b. The initial value of salinity (S_b) was established by observing the trend in the salinity profile directly below the haline bulge; in most cases the salinity trend was very linear and monotonic beneath the bulge, however in general the salinity profiles were less homogeneous than the temperature profiles. After selecting the starting location, the absolute salinity was averaged over 10 meters.

To find the total mass of frazil ice ($Mass_{ice}^{S}$) in the water column, the integral

of each component of the salt ratio is taken over the depth range of the anomaly. This integral is multiplied by the total Mass of Water ($Mass_{Water}^{Total}$) initially in the depth range of the anomaly. The resulting estimates of mass ice produced are listed in Table 1.

$$Mass_{ice}^{S} = Mass_{Water}^{Total} * \frac{\int_{z=0}^{z=H} \Delta S \, dz}{\int_{z=0}^{z=H} Sobs \, dz} \quad (3)$$

$$Mass_{Water}^{Total} = \rho_b * A * \int_{z=0}^{z=H} dz \quad (4)$$

A more detailed explanation of equations 3 and 4 is contained in Supplemental 3.

4.3 Summary of the Mass of Ice derived from Temperature and Salinity

An appreciable volume of frazil ice growth in supercooled water gave rise to salt rejection near the ocean surface, as depicted in the salinity profiles (Figure 7). The derived masses of ice are listed in Table 1. We estimate between 5.8 and 0.13kg of frazil ice were formed, depending on whether temperature (§ 4.1) or salinity (§ 4.2) anomalies are used for the budget.

It is noteworthy that the salt inventories estimate between 2 and 6 times more frazil ice than temperature inventories. The smaller amount of ice derived from the heat inventory calculation is likely caused by atmospheric heat loss. Whereas, the salt rejected by frazil ice can only mix into the ocean, the heat produced by frazil ice can quickly escape to the very cold atmosphere, which is driving much of the super-cooling in the first place. Additionally, the salinity calculation assumed no evaporation. Evaporation would contribute to excess salinity; however it would also decrease the temperature. Given the positive temperature anomaly and high relative

humidity (on average 78.3%), the effects of evaporation on salinity were neglected. The effects of evaporation would reduce the mass of ice derived from the salinity anomaly, however, Mathiot et al (2012) found that evaporation was secondary to ice production and contributed a mere 4% to salt flux. Because the heat budget has an extra loss term that we are not able to easily quantify, we suggest that ice mass from the heat inventory significantly underestimates frazil growth as compared to the salt inventory.

Table 1: CTD Stations with anomalous maxima and derived ice mass, showing maximum values of the temperature anomaly, mass of ice derived from the temperature anomaly (§4.1), maximum value of the salinity anomaly, and mass of ice derived from the salinity anomaly (§4.2).

Station	Date and Time	Maximum Δ T (°C)	$Mass_{ice}^{T}$ (kg)	Maximum ΔS (g kg^{-1})	$Mass_{ice}^{S}$ (kg)
25	May 03 23:00:41	0.009	0.554	0.004	1.042
26*	May 06 02:30:08	0.008	0.406	--	---
27	May 06 13:08:11	0.005	0.349	0.003	1.979
28	May 06 17:59:12	0.007	0.277	0.004	0.427
29	May 07 15:29:32	0.004	0.250	0.007	1.267
30	May 09 07:28:24	0.007	0.205	0.005	4.207
32	May 09 18:24:56	0.008	0.367	0.007	5.778
33**	May 10 05:16:29	---	---	0.004	0.734
34	May 10 20:16:46	0.004	0.129	0.005	1.572
35	May 11 00:56:32	0.012	0.698	0.016	4.793
40	May 17 04:02:37	0.006	0.705	0.003	0.906

*Station 26 did not have a measurable salinity anomaly but was included due to the clarity of the temperature anomaly. Conversely, **Station 33 did not have a

measurable temperature anomaly but was included due to the clarity of the salinity anomaly.

5.0 INTERPRETING THE LIFETIME OF THE ANOMALIES

One question that arises while trying to understand these T and S anomalies is how to interpret their persistence or lifetime: are they short-lived or do they represent an accumulation over some longer ice formation period? One interpretation is that the anomalies begin to form at the onset of the katabatic wind event, implying that the time required to accumulate the observed heat and salt anomalies is similar to that of a katabatic wind event (e.g. 12-48 hours). This, in turn would suggest that the estimated frazil ice production occurred over the lifetime of the katabatic wind event. Another interpretation is that the observed anomalies reflect the near-instantaneous production of frazil ice. In this scenario, heat and salt are simultaneously produced and actively mixed away into the far field. In this case, the observed temperature and salinity anomalies reflect the net difference between production and mixing. One way to address the question of lifetime is to ask, "if ice production stopped, how long would it take for the heat and salt anomalies to dissipate?" The answer depends on how vigorously the water column is mixing, therefore in this section we examine the mixing rate. We can first get some indication of the lifetime by simply examining the density profiles.

5.1 An apparent instability in each density profile

Initially, we expected buoyancy production from excess heat to effectively offset the buoyancy loss from excess salt within each anomaly. The result would be a stably stratified or at least neutrally buoyant water column. This seemed most likely, because the conventional interpretation is that, even though a profile may appear

unstable in T or in S, an unstable density profile is swiftly destroyed by convective instability. Instead, the majority of the 11 profiles revealed that temperature did not compensate for salinity, leading to observations of an unstable water column. This suggests that dense, saline water near the surface was producing an unstable water column (Figure 10). These density profiles are extremely unusual as any such instability will result in rapid vertical mixing and redistribution of the density anomaly, usually evading direct observation by CTD.

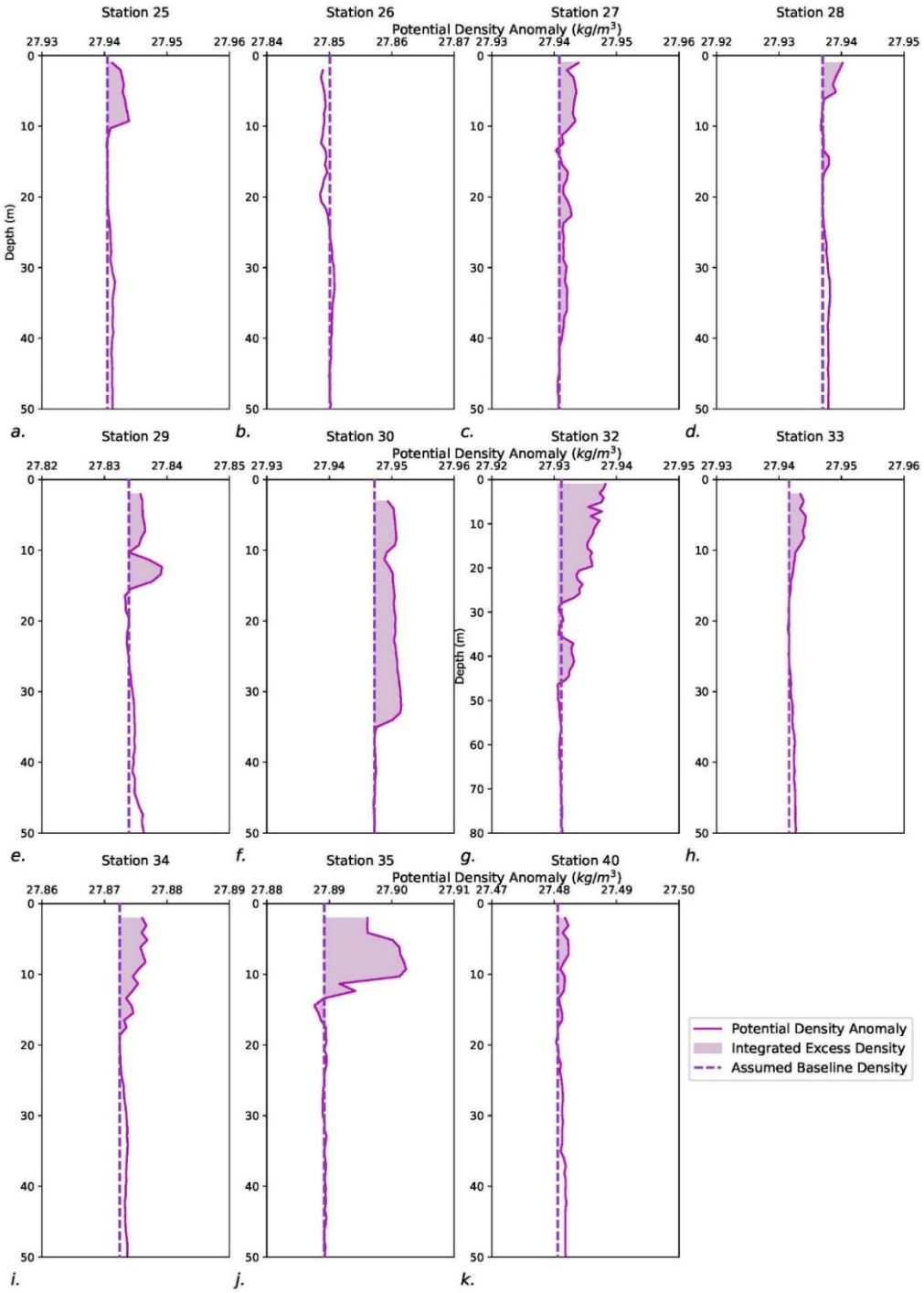

Figure 10: Potential density anomalies (potential density minus 1000 kg m^{-3}) with a reference pressure of 0 dbars for all 11 stations. The integrated excess density and assumed baseline density are depicted to highlight the instability. b) Station 26 does not present a density anomaly because it does not have a salinity anomaly. In the absence of a salinity anomaly, the temperature anomaly creates an area of less dense water, or a stable anomaly.

We hypothesize that an unstable water column that persists long enough to be profiled, must be the result of a continuously produced instability. The katabatic winds appeared to dynamically maintain these unstable profiles, through continual ice production leading to the observed heat and salt excesses at a rate that exceeds the mixing rate. If the unstable profiles reflect a process of continuous ice production, then the "inventory" of ice that we infer from our simple heat and salt budgets must reflect ice production during a relatively short period of time, defined by the time it would take to mix the anomalies away, once ice production stopped.

Similarly, Robinson et al (2017) found that brine rejection from platelet ice formation (§3.5) also leads to dense water formation and a static instability. Frazil ice formation from continually supplied Ice Shelf Water (ISW) created a stationary instability, which was observable before being mixed by convection to the underlying homogeneous water column that extended to 200 meters. Similarly, the katabatic winds and cold air temperatures continually supply supercooled water to the polynya supporting the instability.

5.2 Relating the lifetime to turbulent eddy mixing

In the polynya the katabatic winds produce turbulent vertical eddies that continuously stir the water and disperse the excess temperature and salinity from frazil ice production into the homogeneous mixed layer found below the anomalies. The turbulence is composed of varying size and strength eddies. The largest eddies regulate the rate of dispersion (Cushman-Rosin, 2019). A characteristic timescale, *t,*

can be approximated by relating the largest eddy size and the rate of turbulent kinetic energy dissipation (Cushman-Rosin, 2019).

$$t \approx \frac{d}{(\varepsilon\, d)^{\frac{1}{3}}} \approx \left(\frac{d^2}{\varepsilon}\right)^{\frac{1}{3}} \quad (5)$$

Here, d is the characteristic length of the largest eddy and ε is the turbulent kinetic energy dissipation rate. In this section we discuss and select the best length scale in an environment dominated by buoyancy and wind shear. We then estimate and quantify environmental parameters critical to the length and characteristic time scale calculation. Next, we will return to and solve for the length scale and lastly we will solve for the characteristic timescale.

5.2.1 Estimating the length scale in a environment driven by buoyancy and wind shear

Before we can evaluate equation 5 and determine the lifetime, we needed to identify the length of the largest eddies which requires a heuristic argument in order to establish a single length scale. The largest eddies can be as large as "the domain"; in the water column, the domain might be as large as the mixed-layer (MLD), up to 600 m in some of the PIPERS profiles. However, a homogenous mixed-layer does not imply active mixing throughout the layer (Lombardo and Gregg, 1989). On the other hand, the length of each salinity anomaly was easy to establish but does not necessarily reflect the maximum eddy size. For reference the MLDs and depth of the salinity anomalies are listed in Table 2.

Instead, the most characteristic length scale in an environment driven by both buoyancy and wind shear is the Monin-Obukhov length (L_{M-O}) (Monin-Obukhov, 1954). When L_{M-O} is small, buoyant forces are dominant and when L_{M-O} is large, wind

shear forces are dominant. While theL_{M-O}can be expressed using several different estimates of shear and buoyancy, we focus on the salt-driven buoyancy flux, because those anomalies come closest to capturing the process of frazil ice production (see §4.3 for more detail).

$$L_{M-O} = -\frac{u_*^3}{k\beta g w \underline{\Delta S}} \tag{6}$$

where $u_*$is the wind-driven friction velocity at the water surface,$g$is gravitational acceleration, *w* is the water vertical velocity ΔS is the salt flux, $\beta$is the coefficient of haline contraction, and $k$is the von Karman constant. A more detailed explanation and the specific values are listed in Supplemental 4.

5.2.2 Estimation and Quantification of Input Environmental parameters

To solve for the length of the largest eddy using equation 6, we used the NB Palmer wind speed record, adjusted to the 10 m reference a log-wall profile (Manwell et. al, 2010). Roughness class 0 (z_0) was used in the calculation which is associated with water and has a roughness length of 0.0002 m.

$$U_{10} = U_{palmer} * \frac{ln(\frac{z}{z_o})}{ln(\frac{z_{pamler}}{z_o})} \tag{7}$$

The wind speed at 10 meters is U_{10} , $U_{palmer}$is the NB Palmer wind speed, measured at a masthead height of $z_{palmer} = 24\ m$. Together, these values determine the wind stress, τ as,

$$\tau = C_D\ \rho_{air} U_{10}^2 \tag{8}$$

where ρ_{air} represents the density of air, with a value of 1.3406 kg m^{-3} calculated using averages from NB Palmer for air temperature (-18.73 ℃), air pressure (979.4 mbars), and relative humidity (78.3%). C_D represents a dimensionless drag coefficient and was calculated as 1.525 x 10^{-3}, using COARE 3 code, modified to incorporate wave height and speed (Fairall et al, 2003). The average weather data from NB Palmer was paired with the wave height and wave period averaged from 04 May SWIFT to find C_D. A more detailed explanation and the specific values are listed in Supplemental 5.

Once we found the wind stress, we could determine the aqueous friction velocity (u_*) at the air-sea interface using as follows:

$$u_* = \sqrt{\frac{\tau}{\rho_{water}}} \tag{9}$$

We used the Surface Wave Instrument Float 21 with Tracking (SWIFT), to measure waves, winds, and turbulence (Thomson, 2012; Thomson et al, 2016; Zippel et al 2016). Using SWIFT buoys, vertical velocity and turbulent kinetic energy dissipation rates, during ocean wave timeline breaking, can be estimated. SWIFT deployments occurred during the period of CTD observations, as shown in supplemental figure 2, timeline of events. The SWIFT deployments do not always coincide in time and space with the CTD profiles, so some effort was made to associate the most relevant profile based on wind speed. The averaged wind speed at all of the CTD stations with anomalies was 10.2 m s^{-1}. For the May 2, May 4, May 7 and May 9 SWIFT deployments, the wind speeds are 21.67 m s^{-1}, 9.36 m s^{-1}, 17.25 m

s^{-1}, and 20.05 m s^{-1} respectively. Based on the wind speeds, May 04 was the most comparable to the CTD stations.

SWIFT data from May 4 was averaged for Turbulent Kinetic Energy (TKE) dissipation and vertical velocity (w). The vertical velocity (w) was measured in the upper meter of the column and based on those buoy deployments, an average value of w= 0.015 m $s^{-1}$was selected. An average value of ε=1.85 x 10^{-5} m^2 $s^{-3}$was used for dissipation of TKE.

5.2.3 Resolving the length and time scale of turbulent mixing

Following estimation of the environmental parameters, equation 6 can be solved for the L_{M-O}. For these calculations a value of 0.41 was used for the von Karman constant, k. Haline contraction, β, was calculated from Gibbs Seawater toolbox and averaged over the depth range of the anomaly. The excess salt, $\underline{\Delta S}$, was found using the average value of ΔS for each profile anomaly. The values of L_{M-O}range from 6-330 m (Table 2). The large value indicates that wind shear forces are dominant. In general, the $L_{M-O}$was longer than the salinity anomaly but smaller than the mixed layer depth. Station 35, the station with the largest salinity anomaly and highest mass of ice derived from salinity has $L_{M-O}$of 6 meters, much smaller than other stations. This indicates that at Station 35 buoyant forces are more dominant than other stations.

Using the L_{M-O}, the estimates of TKE dissipation rate (ε) can be applied to find the characteristic time scale or lifetime using equation 5. The rates of mixing

raged from 2 to 29 minutes, vary by one order of magnitude, and have a 14 minute average.

6.0 RATE OF FRAZIL ICE PRODUCTION IN TERRA NOVA AND ROSS POLYNYAS

To calculate the frazil ice production rate, we focus on the mass of ice estimates that are derived from salt inventories. This is justified by the systematically smaller estimates of ice mass that are derived from the heat inventory (see §4.3). We attribute the smaller values to heat loss to the atmosphere. The frazil ice production rate is calculated using the estimates of ice mass taken from salt inventories ($Mass_{ice}^{S}$) and using the mixing lifetime (t) that was determined from TKE dissipation in §5.

$$Production\ rate\ = \frac{Mass_{ice}^{S}}{t * \rho_{ice} * A} \quad (10)$$

Here, $\rho_{ice} = 920$ kg m^{-3}, t=lifetime, in days, and $A = 1\ m^2$. The results are summarized in Table 2. A more detailed explanation and the specific values are listed in Supplemental 6.

6.1 Variability in the frazil ice production rate

The ten estimates of frazil ice production rate ranged from 7 to 358 cm day^{-1}. These sea ice production rates show some spatial trends within the Terra Nova Bay polynya that correspond with conditions as we understand them, in different parts of the polynya. As shown in Figure 11, a longitudinal gradient emerges along the axis of the TNBP when looking at a subsection of stations (Station 30, 32, and 25/33). Beginning upstream near the Nansen Ice shelf (30) and downstream along the polynya axis, to the northeast, the ice production rate decreases. The upstream production rate

is 56 cm day^{-1} followed by midstream values of 31 cm day^{-1}, and lastly downstream values of 9 cm day^{-1}. This pattern is similar to the pattern modeled by Gallee (1997). The production rate at Station 35, was significantly higher than all other stations production rate, but this large excess is reflected in both the heat and salt anomalies. The excess salt value is 260% greater than the closest station in both time and quantity, Station 34.

While none of the CTD casts were in the exact same location, there were 3 pairs of stations located in close geographic proximity (see Figure 11): stations 25 and 33, stations 26 and 30, and station 27 and 28. Station 25 and Station 33 were in the same geographic location and had very similar production rates of 9.82 cm day^{-1}and 8.85 cm day^{-1}. The U_{10} wind speed from Station 25 was 11.77 m s^{-1} while the wind speed from Station 33 was 7.74 m s^{-1}. Station 26 and 30 were located near each other, however Station 26 did not present with a salinity anomaly. Station 27 and 28 were located in a similar location. Station 27 had a production rate of 17.77 cm day $-$ 1,while Station 28 had a production rate of 7.61cm day^{-1}. The U_{10} wind speed from Station 27 was 10.68 m s^{-1} while the wind speed from Station 28 was 5.89 m s^{-1}. The relationship of Station 27 to Station 28, and Station 25 to Station 33 support a direct relationship between wind speed and ice production rate. However, some of the pairings do not follow this trend. Station 26 did not present a salinity anomaly. Station 35 and 34, the next two closest stations have drastically different ice production rates. This anomaly and other variations are attributed to the underlying assumption of neglecting advection. Other variations are due to small mesoscale fronts, eddies and

other flow structures that can produce variability that is not easily explained with coarse sampling.

Table 2: Summary of mass of ice derived from salinity, lifetime, and production rates.

Station	$Mass_{ice}^{S}$ (kg)	Salinity anomaly depth (m)	L_{M-O} (m)	Est MLD (m)	Lifetime (min)	Production rate (cm/day)
25	1.042	13.4	140.59	350	16.60	9.82
26*	---	--	--	100	---	---
27	1.979	41.2	151.26	500	17.43	17.77
28	0.427	17.5	54.12	600	8.78	7.61
29	1.267	21.6	80.00	275	11.40	17.40
30	4.207	36	83.45	500	11.73	56.16
32	5.778	47	223.9	375	22.64	39.95
33	0.74	23.7	98.38	500	13.09	8.85
34	1.572	19.6	65.56	175	9.98	24.65
35	4.793	14.4	6.30	150	2.09	358.27
40	0.906	18.6	174.61	120	19.18	7.39

*Station 26 does not have a measurable salinity anomaly and a production rate could not be calculated via this method.

6.2 How do these production rates compare to prior modeled and field estimates?

Calculated production rates from PIPERS ranged from 7 to 359 cm day^{-1} and are plotted in Figure 11. Station 40, the one station in RSP, represents the minimum frazil ice production rate. While there is only one data point in RSP and variability in the TNBP, TNBP was expected to outpace RSP in production. The median, 13.65 cm day^{-1}, very closely matches Schick et al (2018) estimated average ice production rate for the month of May 16.8 cm day^{-1}calculated using heat fluxes. Kurtz and Bromwich (1985) estimated average ice production at 30 cm $day^{-1}$for the month of May by deriving an ice production rate from heat budget analysis.

The remaining published production rates are winter averages. Our mean production rate, 52.05 cm $day^{-1}$is comparable to Sansiviero et al (2017), who modeled a wintertime maximum rate of 48.08 cm day^{-1} using a sea-ice model. It is similarly comparable to Gallee (1997) modeled results for a polynya. Gallee (1997) modeled in three dimensions over four days and mapped daily ice production rates in TNBP. Modeled ice production rates near the coast (e.g. station 35) were 50 cm day^{-1}, decreasing to 0 cm day^{-1} downstream and at the outer boundaries. Station 35 is located closest to the coast (see Figure 11 in the region where highest modeled production rates took place Gallee (1997). Petrelli et al. (2008) modeled a wintertime maximum production rates of 26.4 cm day^{-1}using a coupled atmospheric-sea ice model. Fusco et al (2002) applied a classic model for latent heat polynyas and modeled production rates at 85 cm day^{-1} for 1993 and 72 cm day^{-1} for 1994. We might expect our production rates to be lower than the median of prior estimates, considering that the PIPERS expedition took place in late autumn when the polynya has typically not yet

reached its maximum production rate. While some of our production rates far exceed modeled results, we attribute some of that variability to the relatively short time scale of these ice production "snapshots". As our estimates integrate over minutes to hours, instead of days to months they are more likely to capture the high frequency variability in this ephemeral process. As the katabatic winds oscillate, the polynyas enter periods of slower ice production, driving average rates down.

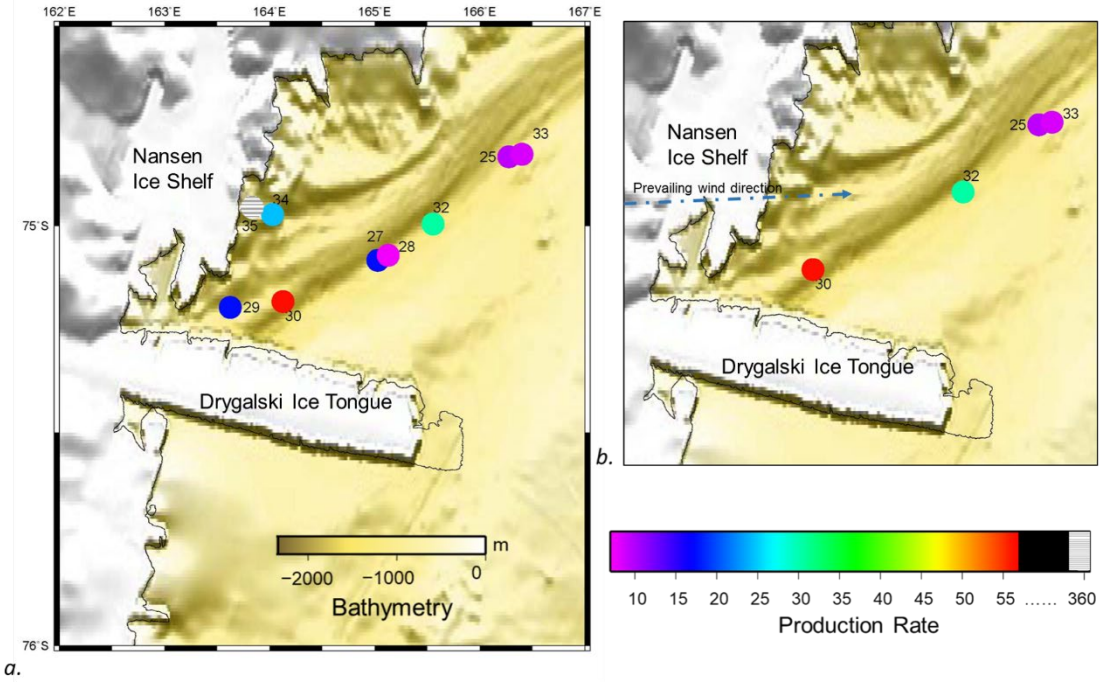

Figure 11: TNBP map of ice production rates. a). Map of TNBP ice production rates, rainbow color bar indicates the ice production rate in cm day^{-1} and ranges from 7-57 cm day^{-1} . Station 35, marked as an outlier and not included in the color bar, is displayed with a patterned white marker. b). A cross-section of TNBP stations displayed to highlight a spatial pattern of decreasing ice production rates while moving away from the Nansen Ice shelf. The prevailing wind direction is noted in a dashed blue arrow.

7. CONCLUSIONS

The goal of PIPERS was to study polynyas, ice production, and seasonal evolution in the Ross Sea. During the late autumn cruise and katabatic wind events in the Terra Nova Bay polynya and the Ross Sea polynya, unexpected temperature and salinity anomalies provided an in-situ method of quantifying ice production rate. Polynyas have been regarded as ice production factories with a wide range of model estimated production rates. Traditionally it has been hard to quantitatively estimate ice production due to the challenges of obtaining in-situ ice measurements (Tamura et al, 2017). In-situ salinity and temperature anomalies observed at 11 CTD stations were correlated to frazil ice formation and used to estimate polynya ice production. Sea ice production rates vary from 7 to 360 cm day^{-1}, a wide range. We suggest this is because we are capturing production on short timescales (minutes). The method demonstrated in this study provides an in-situ process for estimating sea ice production more accurate production rates can be obtained via our method by temporal spread of CTD casts in the same spatial location.

The Ross Sea polynyas have high production rates and are significant contributors to Antarctic Bottom Water formation. As shown in our production rates per area, TNBP has higher production rates than RSP. However, the significantly larger size of the RSP leads it to have the highest overall ice production rate of any Antarctic polynya (Tamura et al, 2017). Since 2015, the overall sea ice extent around Antarctica has decreased, with 2017 being an abnormally low year (Supplemental Figure 4). Better understanding ice production in the Ross Sea polynyas will help understand the Southern Ocean trend. A decrease in ice production rate correlates to freshening of Antarctic bottom water which would have global impacts.

8. REFERENCES

Armstrong, T. (1972). *World Meteorological Organization. WMO sea-ice nomenclature. Terminology, codes and illustrated glossary. Edition 1970. Geneva, Secretariat of the World Meteorological Organization, 1970, [ix], 147 p. [including 175 photos] + corrigenda slip. (WMO/OMM/BMO, No. 259, TP. 145.)*. *Journal of Glaciology - J GLACIOLOGY* (Vol. 11). https://doi.org/10.1017/S0022143000022577

Bromwich, D. H., & Kurtz, D. D. (1984). Katabatic wind forcing of the Terra Nova Bay polynya. *Journal of Geophysical Research*, *89*(C3), 3561. https://doi.org/10.1029/JC089iC03p03561

Buffoni, G., Cappelletti, A., & Picco, P. (2002). An investigation of thermohaline circulation in Terra Nova Bay polynya. *Antarctic Science, 14*(1), 83-92. doi:10.1017/S0954102002000615

Coachman, L. K. (1966), Production of supercooled water during sea ice formation, in *Proceedings of the Symposium on Arctic Heat Budget and Atmospheric Circulation*, pp. 497–529, RAND Corp., Santa Monica, Calif.

Comiso J.C. & Gordon A.L. (1998). Inter-annual variability in summer sea ice minimum, coastal polynyas and bottom water formation in the Weddell Sea. In M.O. Jeffries (ed): Antarctic sea ice: physical processes, interactions and variability. Pp. 293–315. Washington DC: American Geophysical Union.

Cox, G. F. N., & Weeks, W. F. (1983). Equations for determining the gas and brine volumes in sea-ice samples. *Journal of Glaciology* (Vol. 29). Retrieved from https://www.igsoc.org/journal/29/102/igs_journal_vol29_issue102_pg306-316.pdf

Cushman-Rosin, B. (2019). *Environmental Fluid Mechanics*. New York: John Wiley & Sons.

Dmitrenko, I. A., Wegner, C., Kassens, H., Kirillov, S. A., Krumpen, T., Heinemann, G., … Busche, T. (2010). Observations of supercooling and frazil ice formation in the Laptev Sea coastal polynya. *Journal of Geophysical Research*, *115*(C5), C05015. https://doi.org/10.1029/2009JC005798

Fairall, C.W., E.F. Bradley, J.E. Hare, A.A. Grachev, and J.B. Edson (2003), Bulk parameterization of air sea fluxes: updates and verification for the COARE algorithm, J. Climate, 16, 571-590.

Fetterer, F., K. Knowles, W. N. Meier, M. Savoie, and A. K. Windnagel. 2017, updated daily. *Sea Ice Index, Version 3*. Sea Ice Index, Version 3. Boulder, Colorado USA. NSIDC: National Snow and Ice Data Center. doi: https://doi.org/10.7265/N5K072F8. 09 March 2019.

Fusco, G., Flocco, D., Budillon, G., Spezie, G., & Zambianchi, E. (2002). Dynamics and variability of Terra Nova Bay polynya. Marine Ecology, 23(SUPPL. 1), 201–209. https://doi.org/10.1111/j.1439-0485.2002.tb00019.x

Fusco, Budillon, & Spezie. (2009). Surface heat fluxes and thermohaline variability in the Ross Sea and in Terra Nova Bay polynya. Continental Shelf Research, 29(15), 1887-1895.

Gallée, H. (1997). Air-sea interactions over Terra Nova Bay during winter: Simulation with a coupled atmosphere-polynya model. *Journal of Geophysical Research: Atmospheres*, *102*(D12), 13835–13849. https://doi.org/10.1029/96JD03098

Heorton, H. D. B. S., & Feltham, D. L. (n.d.). A Model of Sea Ice Formation in Leads and Polynyas. https://doi.org/10.1175/JPO-D-16-0224.1

Ito, M., Ohshima, K. I., Fukamachi, Y., Simizu, D., Iwamoto, K., Matsumura, Y., … Eicken, H. (2017). Observations of supercooled water and frazil ice formation in an Arctic coastal polynya from moorings and satellite imagery. https://doi.org/10.3189/2015AoG69A839

Jacobs, S. (2004). Bottom water production and its links with the thermohaline circulation. *Antarctic Science, 16*(4), 427-437. doi:10.1017/S095410200400224X

Jenkins, A., & Bombosch, A. (1995). Modeling the effects of frazil ice crystals on the dynamics and thermodynamics of Ice Shelf Water plumes. *Journal of Geophysical Research*, *100*(C4), 6967. https://doi.org/10.1029/94JC03227

Jones, D. W. R., & Wells, A. J. (2018). Frazil-ice growth rate and dynamics in mixed layers and sub-ice-shelf plumes. *The Cryosphere*, *12*, 25–38. https://doi.org/10.5194/tc-12-25-2018

Kurtz, D. D., & Bromwich, D. H. (1985). A Recurring, Atmospherically forced polynya in terra nova bay. Oceanology of the Amarcric Cominenral Shelf Antarctic Research Series (Vol. 43).

Li, N., Kinzelbach, W., Li, W., & Dong, X. (2015). Box model and 1D longitudinal model of flow and transport in Bosten Lake, China. *Journal of Hydrology*, *524*, 62–71. https://doi.org/10.1016/J.JHYDROL.2015.02.032

Lombardo, C., & Gregg, M. (1989). Similarity scaling of viscous and thermal dissipation in a convecting surface boundary layer. *Journal of Geophysical Research, 94*(C5), 6273-6284.

Mathiot, P., Jourdain, N., Barnier, C., Gallée, B., Molines, H., Sommer, J., & Penduff, M. (2012). Sensitivity of coastal polynyas and high-salinity shelf water production in the Ross Sea, Antarctica, to the atmospheric forcing. Ocean Dynamics, 62(5), 701-723.

Manwell, J. F., McGowan, J. G., & Rogers, A. L. (2010). Wind Energy Explained: Theory, Design and Application.

Manzella, G. M. R., R. Meloni, and P. Picco, Current, temperature and salinity observations in the Terra Nova Bay polynya area, in Oceanography of the Ross Sea, edited by G. Spezie and G. M. R. Manzella, pp 165-173, Springer-Verlag, New York, 1999.

Martin, S., Drucker, R. S., & Kwok, R. (2007). The areas and ice production of the western and central Ross Sea polynyas, 1992-2002, and their relation to the B-15 and C-19 iceberg events of 2000 and 2002. *Journal of Marine Systems.* https://doi.org/10.1016/j.jmarsys.2006.11.008

Matsumura, Y., & Ohshima, K. I. (2015). Lagrangian modelling of frazil ice in the ocean. *Annals of Glaciology*, *56*(69), 373–382. https://doi.org/10.3189/2015AoG69A657

Michel, B. (1967). Physics of Snow and Ice: Morphology of Frazil Ice (Vol. 1, pp. 119–128).

Monin, A. S., & Obukhov, A. M. (1954). Basic laws of turbulent mixing in the surface layer of the atmosphere. *Contrib. Geophys. Inst. Acad. Sci. USSR*, *151*(163), e187.

Morales Maqueda, M. A., Willmott, A. J., & Biggs, N. R. T. (2004). Polynya Dynamics: a Review of Observations and Modeling. *Reviews of Geophysics*, *42*(1), RG1004. https://doi.org/10.1029/2002RG000116

Orsi, & Wiederwohl. (2009). A recount of Ross Sea waters. Deep-Sea Research Part II, 56(13), 778-795.

Overland, J. E. (1985). Atmospheric boundary layer structure and drag coefficients over sea ice. Journal of Geophysical Research, 90(C5), 9029–9049. https://doi.org/10.1029/JC090iC05p09029

Park, J., Kim, H.-C., Jo, Y.-H., Kidwell, A., & Hwang, J. (2018). Multi-temporal variation of the Ross Sea Polynya in response to climate forcings. *Polar Research*, *37*(1), 1444891. https://doi.org/10.1080/17518369.2018.1444891

Pease, C. H. (1987). The size of wind-driven coastal polynyas. *Journal of Geophysical Research*, *92*(C7), 7049. https://doi.org/10.1029/JC092iC07p07049

Petrelli, P., Bindoff, N.L., Bergamasco, A., 2008. The sea ice dynamics of Terra Nova Bay and Ross Ice Shelf Polynyas during a spring and winter simulation. J. Geophys. Res.

Roberts, P. J., & Webster, D. R. (2002). *Turbulent diffusion*(pp. 7-47). ASCE Press, Reston, Virginia.

Sansiviero, M., Morales Maqueda, M. Á., Fusco, G., Aulicino, G., Flocco, D., & Budillon, G. (2017). Modelling sea ice formation in the Terra Nova Bay polynya. *Journal of Marine Systems*, *166*, 4–25. https://doi.org/10.1016/J.JMARSYS.2016.06.013

SBE 911plus CTD | Sea-Bird Scientific USA - Downloads | Hach. (n.d.). Retrieved August 15, 2018, from https://www.seabird.com/profiling/sbe-911plus-ctd/family-downloads?productCategoryId=54627473769

Skogseth, R., Nilsen, F., & Smedsrud, L. H. (2009). Supercooled water in an Arctic polynya: observations and modeling. Journal of Glaciology, 55(189), 43–52. https://doi.org/10.3189/002214309788608840

Talley, L.D., Picard, G.L., Emery, W.J. Swift, J.H. *Physical Properties of Seawater 3.1. Molecular properties of water*. (2011).

Tamura, T., Ohshima, K. I., & Nihashi, S. (2008). Mapping of sea ice production for Antarctic coastal polynyas. Geophysical Research Letters, 35(7), 1–5. https://doi.org/10.1029/2007GL032903

Thomson, J. (2012). Wave breaking dissipation observed with “swift” drifters. Journal of Atmospheric and Oceanic Technology, 29(12), 1866–1882. https://doi.org/10.1175/JTECH-D-12-00018.1

Thomson, J. (2012). Wave breaking dissipation observed with “swift” drifters. Journal of Atmospheric and Oceanic Technology, 29(12), 1866–1882. https://doi.org/10.1175/JTECH-D-12-00018.1

Tsang, G., O ’, T., & Hanley, D. (1985). Frazil formation in water of different salinities and supercoolings. *Journal Of Glaciology*, *31*(108).

Ushio S., & Wakatsuchi, M. (1993). a Laboratory Study on Supercooling and Frazil Ice Production Processes in Winter Coastal Polynyas. *Journal Of Geophysical Research-Oceans*, *98*(C11), 20321–20328. https://doi.org/10.1029/93JC01905

Van Woert, M. L., The wintertime expansion and contraction of the Terra Nova Bay polynya, in Oceanography of the Ross Sea: Antarctica, edited by G. Spezie and G. M. R. Manzella, pp. 145-164, Springer-Verlag, New York, 1999a

Van Woert, M. L., Wintertime dynamics of the Terra Nova Bay polynya, J. Geophys. Res., 104, 7753-7769, 1999b.

Wakatsuchi, M., & Ono, N. (1983). Measurements of salinity and volume of brine excluded from growing sea ice. *Journal of Geophysical Research*, *88*(C5), 2943. https://doi.org/10.1029/JC088iC05p02943

Wilchinsky, A. V., Heorton, H. D. B. S., Feltham, D. L., Holland, P. R., Wilchinsky, A. V., Heorton, H. D. B. S., … Holland, P. R. (2015). Study of the Impact of Ice Formation in Leads upon the Sea Ice Pack Mass Balance Using a New Frazil and Grease Ice Parameterization. *Journal of Physical Oceanography*, *45*(8), 2025–2047. https://doi.org/10.1175/JPO-D-14-0184.1

APPENDICES

Appendix 1: Supplemental 1: Estimation of frazil ice concentration using temperature anomalies

To measure the amount of the temperature anomaly:

$$\Delta T = T_{obs} - T_b \quad \text{(S1.1)}$$

T_{obs} =in-situ conservative temperature within the anomaly (℃)

T_b =baseline or far field temperature (10 meter average below anomaly)(℃)

* ΔT=℃ = degrees K

substituted.

Heat content per volume of water can be quantified as Q and calculated (Talley et al 2011). All thermodynamic properties of seawater were evaluated via the Gibbs Seawater toolbox which uses the International Thermodynamic Equation of Seawater – 2010 (TEOS-10).

$$Q = \rho C_p T \quad \text{(S1.2)}$$

ρ =seawater density (kg m^{-3})

C_p= specific heat capacity (J kg^{-1} K^{-1})

T= temperature of the water (degrees K)

Q= heat content per volume (J m^{-3})

To find the heat content in the temperature anomaly, or excess heat, equation S1.1 can be substituted into equation S2.2.

$$Q_{excess} = \rho\, C_p\, \Delta T \qquad \text{(S1.3)}$$

ΔT=amount of Temperature anomaly (degrees K)

$Q_{excessl}$ = excess heat content per volume (J m^{-3})

To find the total mass amount of heat in the water column, the integral of $Q_{residual}^{total}$ is taken over the depth range of the anomaly (z) and multiplied by the assumed that the horizontal area (A) captured by the CTD was 1 m^2.

$$Q_{excess}^{total} = \int_{z=0}^{z=H} \rho\ \ C_p\ \ \Delta T\ \ dz\ * A \qquad \text{(S1.4)}$$

A= Area= 1 m^2

H= depth of the Anomaly (m)

Q_{excess}^{total}= total amount of residual heat in the water column (J)

The mass of frazil ice is estimated by applying the Latent heat of formation as a conversion factor to the calculated internal energy (Q_{excess}^{total}):

$$Mass_{ice}^{temp} = \frac{Q_{excessl}^{total}}{L_f} \qquad \text{(S1.5)}$$

L_f = latent heat of fusion = 3.3 x 10^5 J kg^{-1}

$Mass_{ice}^{temp}$= mass of frazil ice (kg) from temperature derivation

Table S1: Data for frazil ice concentration using temperature anomalies. Includes Baseline Temperature, Density, Depth of the Temperature anomaly, Average Specific Heat Capacity (over the range of the anomaly), Residual heat, and Estimation of Mass of Ice.

Station	T_b(°C)	ρ (kg m^{-3})	H (m)	C_p (J kg^{-1} K^{-1})	Q_{excess}^{total} (J)	$Mass_{ice}^{temp}$ (kg)
25	-1.910	1028.01	11.34	3988.24	182951.55	0.554
26	-1.912	1028.06	24.73	3988.7	121657.07	0.369
27	-1.914	1028.14	15.45	3988.17	115327.03	0.349
28	-1.915	1028.02	15.52	3988.17	91532.01	0.277
29	-1.906	1027.94	11.34	3989.03	82369.7	0.250
30	-1.916	1028.12	8.24	3988.2	67597.98	0.205
32	-1.914	1028.16	11.33	3988.29	121177.9	0.367
33*	-1.913	1028.05	---	3988.27	---	---
34	-1.909	1027.97	13.4	3988.69	42447.42	0.129
35	-1.910	1027.97	19.58	3988.44	230375.69	0.698
40	-1.885	1027.59	20.61	3991.53	232521.55	0.705

* Station 33 does not have a measurable temperature anomaly but has a measurable salinity anomaly so it was included in this table. The specific heat capacity and density value shown area averages of the values used in the calculation. For each depth step of the integral, an individual value unique to that depth was used.

Appendix 2: Supplemental 2: Derivation of Conservation of Mass of Water and Conservation of Mass of Salt

Conservation of Mass of Water:

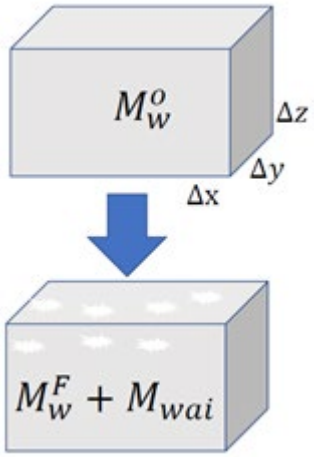

$$M_W^O = M_W^F + M_{wai} \quad \text{(S2.1)}$$

M_W^O =Mass of Water originally

M_W^F =Mass of Water after freezing

M_{wai} =Mass of Water as Ice

Figure S2.1: 1-D box model of the Conservation of Mass of Water.

Conservation of Mass of Salt:

$$M_S^O = M_S^F \quad \text{(S2.2)}$$

Salinity Equations:

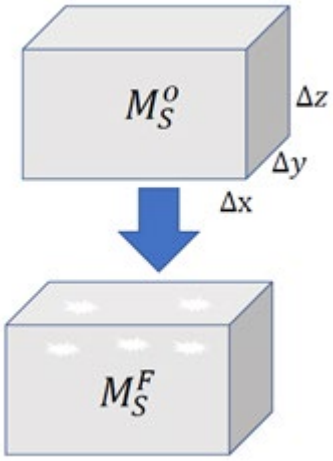

$$M_S^O = S_b * M_W^O \quad \text{(S2.3)}$$

$$M_S^F = S_{obs} * M_W^F \quad \text{(S2.4)}$$

Figure S2.2: 1-D box model of the Conservation of Mass of Salt.

M_S^O =Mass of Salt Initially

M_S^F =Mass of Salt, Final

S_b =Original/Baseline Salinity

S_{obs} = Salinity Final/Observed

Combine the Conservation of Mass of Salt and Salinity Equations, equations S2.2 and S2.3:

$$M_S^F = S_b * M_O^W \quad \text{(S2.5)}$$

Combine S2.5 with Conservation of the Mass of Water S2.1:

$$M_S^F = S_b(M_W^F + M_{wai}) = S_b * M_W^F + S_b * M_{wai} \quad \text{(S2.6)}$$

Combine the Conservation of Mass of Water and the Conservation of Mass of Salt, equations S2.1 and S2.4:

$$M_s^F = S_{obs} * (M_W^O - M_{wai}) = S_{obs} * M_W^O - S_{obs} * M_{wai} \quad \text{(S2.7)}$$

Combine equations from S2.6 and S2.7:

$$S_b * M_W^F + S_b * M_{wai} = S_{obs} * M_W^O - S_{obs} * M_{wai} \quad \text{(S2.8)}$$

Combine equations S2.1 and S2.8:

$$S_b * (M_W^O - M_{wai}) + S_b * M_{wai} = S_{obs} * M_W^O - S_{obs} * M_{wai}$$

$$S_b * M_W^O - S_b * M_{wai} + S_b * M_{wai} = S_{obs} * M_W^O - S_{obs} * M_{wai} \quad \text{(S2.9)}$$

Rearrange equation S2.9 to isolate, $M_O^W and\ M_{wai}$:

$$M_W^O(S_b - S_{obs}) = M_{wai}\ (S_b - S_b - S_{obs}) \quad \text{(S2.10)}$$

Solved equation S2.10 for M_{wai}:

$$M_{wai} = \frac{(S_{obs} - S_b)}{S_{obs}} * M_W^O \quad \text{(S2.11)}$$

Appendix 3: Supplemental 3: Estimation of frazil ice concentration using salinity anomalies

To measure the amount of the salinity anomaly:

$$\Delta S = S_{obs} - S_b \quad \text{(S3.1)}$$

$S_b =$ baseline or far field salinity (10 meter average below anomaly) (g kg^{-1})

S_{obs} = in-situ absolute salinity within the anomaly (g kg^{-1})

ΔS= salinity anomaly (g kg^{-1})

Equation S2.11 solves for the mass of water as ice (M_{wai})at each depth step of the profile.

$$M_{wai} = \frac{(S_{obs} - S_b)}{S_{obs}} * M_W^O \quad \text{(S3.2)}$$

Substitute equation S3.1 into equation S3.2:

$$M_{wai} = \frac{\Delta S}{S_{obs}} * M_W^O \quad \text{(S3.2)}$$

To find the total mass of frazil ice (M_{wai}^T) in the water column, the integral of each component of the salt ratio is taken over the depth range of the anomaly. This integral is multiplied by the total Mass of Water ($M_W^{O,Total}$) initially in the depth range of the anomaly.

$$Mass_{ice}^S = Mass_{Water}^{Total} * \frac{\int_{z=0}^{z=H} \Delta S \, dz}{\int_{z=0}^{z=H} Sobsdz} \quad \text{(S3.3)}$$

$$Mass_{Water}^{Total} = \rho_b * A * \int_{z=0}^{z=H} dz \quad \text{(S3.4)}$$

H= depth of the Anomaly (m)

A= Area= 1 m^2

$Mass_{ice}^S$= total mass of frazil ice (kg) from salinity derivation

$Mass_{Water}^{Total}$=total Mass of Water (kg)

ρ_b= Assumed baseline/initial density, calculated using S_b

Table S2: Data for frazil ice concentration using salinity anomalies. Includes Baseline Salinity, Density, Depth of the salinity anomaly, mass of water assumed to be initially present, and Estimation of Mass of Ice.

Station	$S_b(\frac{g}{kg})$	$\rho_b(\frac{kg}{m^3})$	H (m)	$Mass_{Water}^{Total}$ (kg)	$Mass_{ice}^{S}$(kg)
25	34.861	1028.01	13.40	13771.22	1.042
26	--	1028.06	--	--	---
27	34.962	1028.14	41.22	42379.94	1.979
28	34.867	1028.02	17.52	18007.58	0.427
29	34.730	1027.94	21.64	22242.97	1.267
30	34.870	1028.12	36.07	37080.62	4.207
32	34.849	1028.16	47.40	48738.41	5.778
33	34.863	1028.05	22.67	23305.27	0.734
34	34.778	1027.97	19.58	20126.16	1.572
35	34.798	1027.97	14.43	14829.45	4.793
40	34.293	1027.59	18.55	19062.09	0.906

* Station 26 does not have a measurable salinity anomaly but has a measurable temperature anomaly, so it was included in this table.

Appendix 4: Supplemental 4: Identifying the Length scale

Estimating the maximum dissipation length scale, d_{max}via Monin-Obukhov length (L_{M-O}) (Monin-Obukhov, 1954) to find the size of the largest eddy. The size of the largest eddy or L_{M-O} is used as the vertical mixing length (in meters):

$$L_{M-O} = -\frac{u_*^3}{k\beta g w\underline{\Delta S}} \quad \text{(S4.1)}$$

u_*=friction velocity, calculated in S.4= m s^{-1}

g= gravitational acceleration= 9.81 m s^{-2}

$w\underline{\Delta S}$=salt flux= m g s^{-1} kg^{-1}

w= 0.015 m s^{-1}, (see Section 5.2.1)

$\underline{\Delta S}$= $\frac{\int_{zz=0}^{z=H} \Delta S\, dz}{z}$= g kg^{-1}

β= coefficient of haline contraction, calculated from Gibbs Seawater toolbox and averaged over the depth range of the anomaly

k= von Karman constant= 0.41

$$L_{M-O} = -\frac{u_*^3}{k\beta g w\underline{\Delta S}} = -\frac{\frac{m^3}{s^3}}{k\frac{kg}{g}\frac{m}{s^2}\frac{m}{s}\frac{g}{kg}} = \frac{\frac{m^3}{s^3}}{\frac{m^2}{s^3}} = m \quad \text{(S4.2)}$$

Table S3: Data for Monin-Obukhov Length scale calculations.

Station	$\underline{\Delta S}$ (g kg^{-1})	β	u_* (m s^{-1})	L_{M-O} (m)
25	$2.229x\ 10^{-3}$	$7.867x\ 10^{-4}$	$2.459\ x\ 10^{-2}$	140.59
26	---	---	$2.380\ x\ 10^{-2}$	---
27	$1.546x\ 10^{-3}$	$7.867x\ 10^{-4}$	$2.231\ x\ 10^{-2}$	151.26
28	$7.271x\ 10^{-4}$	$7.867x\ 10^{-4}$	$1.\ 232\ x\ 10^{-2}$	54.12
29	$1.694x\ 10^{-3}$	$7.867x\ 10^{-4}$	$1.860\ x\ 10^{-2}$	80.00
30	$3.503x\ 10^{-3}$	$7.866x\ 10^{-4}$	$2.403\ x\ 10^{-2}$	83.45
32	$3.952x\ 10^{-3}$	$7.866x\ 10^{-4}$	$3.949\ x\ 10^{-2}$	328.38
33	$9.073x\ 10^{-4}$	$7.867x\ 10^{-4}$	$1.618\ x\ 10^{-2}$	98.38
34	$2.287x\ 10^{-3}$	$7.867x\ 10^{-4}$	$1.924\ x\ 10^{-2}$	65.56
35	$8.835x\ 10^{-3}$	$7.867x\ 10^{-4}$	$1.382\ x\ 10^{-2}$	6.30
40	$1.358x\ 10^{-3}$	$7.869x\ 10^{-4}$	$2.241\ x\ 10^{-2}$	174.61

Appendix 5: Supplemental 5: Wind Analysis

Extrapolation of the wind speed at 10 meters (U_{10}) using the NB Palmer wind speed U_{palmer}:

$$U_{10} = U_{palmer} * \frac{ln(\frac{z}{z_o})}{ln(\frac{z_{pamler}}{z_o})} \quad \text{(S5.1)}$$

z_0 =Roughness Class= 0.0002 m

z_{palmer} = Reference height= 24 m

z =Desired height = 10 m

Average environmental values from NB Palmer used as inputs for COARE 3 to calculate the Drag Coefficient (C_D):

$average\ U_{10} =$ average wind speed= 9.8 m s^{-1}

$average\ T_{air=}$average air temperature = -18.7 ℃

$average\ RH =$ average relative humidity= 78.3 %

$average\ P =$ average air pressure= 979.4 dbar

$average\ T_{water} =$ average water temperature = -1.74 ℃

$average\ R_S =$ average shortwave radiation = -3.56 W m^{-2}

$average\ R_L =$average longwave radiation = 201.2 $\frac{W}{m^2}$

$average\ Lat =$average latitude =-75°

Average wave height and wave period of the 04 May SWIFT deployment used the wave as inputs for COARE 3 to calculate the wave dependent Drag Coefficient (C_D):

$average\ Sig_H$ =average significant wave height= 0.58 m

$average\ T$ =average wave period =4.6 seconds

The average phase speed (c_p) was calculated from the wave period (T)using the formula for deep water dispersion:

$$c_p = \frac{g}{2\,\pi} * T \quad \text{(S5.2)}$$

c_p =average phase speed= 7.2 m s^{-1}

g =gravity, 9.81 m s^{-2}

$average\ T$ =average wave period =4.6 seconds

Based on the average values, the Drag Coefficient (C_D)was found to be: C_D=1.525 x 10^{-3}

The wind stress, τ, was calculated for each CTD station based on the extrapolated wind speed at 10 meters, U_{10} , average air density, and average drag coefficient:

$$\tau = C_D\, \rho_{air} U_{10}^2 \quad \text{(S5.3)}$$

ρ_{air} =density of air=1.34 kg m^{-3} calculated using averages from NB Palmer summarized above.

Using wind stress, we derived the friction velocity (u_*) at the air-sea interface using the wind stress and water density, ρ_{water}.

$$u_* = \sqrt{\frac{\tau}{p_{water}}} \quad \text{(S5.4)}$$

u_* = friction velocity

p_{water} = density of water

Table S4: Data for wind analysis summarized in Supplemental 5.

Station	U_{palmer} (m s^{-1})	U_{10} (m s^{-1})	τ (kg m^{-1} s^{-2})	ρ_{water} (kg m^{-3})	u_* (m s^{-1})
25	12.72	11.77	0.622	1028.01	$2.459\ x\ 10^{-2}$
26	12.31	11.39	0.582	1028.06	$2.380\ x\ 10^{-2}$
27	11.54	10.68	0.512	1028.14	$2.231\ x\ 10^{-2}$
28	6.37	5.89	0.156	1028.02	$1.232\ x\ 10^{-2}$
29	9.62	8.90	0.355	1027.94	$1.860\ x\ 10^{-2}$
30	12.43	11.50	0.594	1028.12	$2.403\ x\ 10^{-2}$
32	20.43	18.90	1.603	1028.16	$3.949\ x\ 10^{-2}$
33	8.37	7.74	0.269	1028.05	$1.618\ x\ 10^{-2}$
34	9.95	9.21	0.380	1027.97	$1.924\ x\ 10^{-2}$
35	7.15	6.61	0.196	1027.97	$1.382\ x\ 10^{-2}$
40	11.59	10.72	0.516	1027.59	$2.241\ x\ 10^{-2}$

Supplemental 6: Calculating the rate of mixing and production rate

Using the L_{M-O}, turbulent kinetic energy (ε) can be applied to find the minimum time scale for mixing:

$$t = \frac{\pi\, d}{v_*} \approx \frac{d}{(\varepsilon\, d)^{\frac{1}{3}}} \approx \left(\frac{L_{M-O}2}{\varepsilon}\right)^{\frac{1}{3}} \quad \text{(S5.1)}$$

t =timescale= s

ε =turbulent kinetic energy dissipation= $1.85\ x\ 10^{-5}$ m^2s^{-3}

L_{M-O}= Monin-Obukhov Length= m

The minimum times scale can be used to calculate an ice production rate:

$$Production\ rate = \frac{M_{wai}^{T}}{t * \rho_{ice} * A} = \text{m day}^{-1} \quad \text{(S5.2)}$$

$$Production\ rate = \frac{meters\ of\ frazil\ ice}{day}$$

M_{wai}^{T} =mass of frazil ice derived from salinity anomaly= kg

t= timescale= day

$\rho_{ice} = 920$ kg m^{-3}

$A = 1\ m^2$

Table S5: Calculation of time scale and production rate.

Station	Mass derived from Salt (kg)	$L_{M-O}(m)$	Timescale (min)	Production rate (cm day^{-1})
25	1.042	140.59	16.60	9.82
26	---	---	---	---
27	1.979	151.26	17.43	17.77
28	0.427	54.12	8.78	7.61
29	1.267	80.00	11.40	17.40
30	4.207	83.45	11.73	56.16
32	5.778	223.9	22.64	39.95
33	0.74	98.38	13.09	8.85
34	1.572	65.56	9.98	24.65
35	4.793	6.30	2.09	358.27
40	0.906	174.61	19.18	7.39

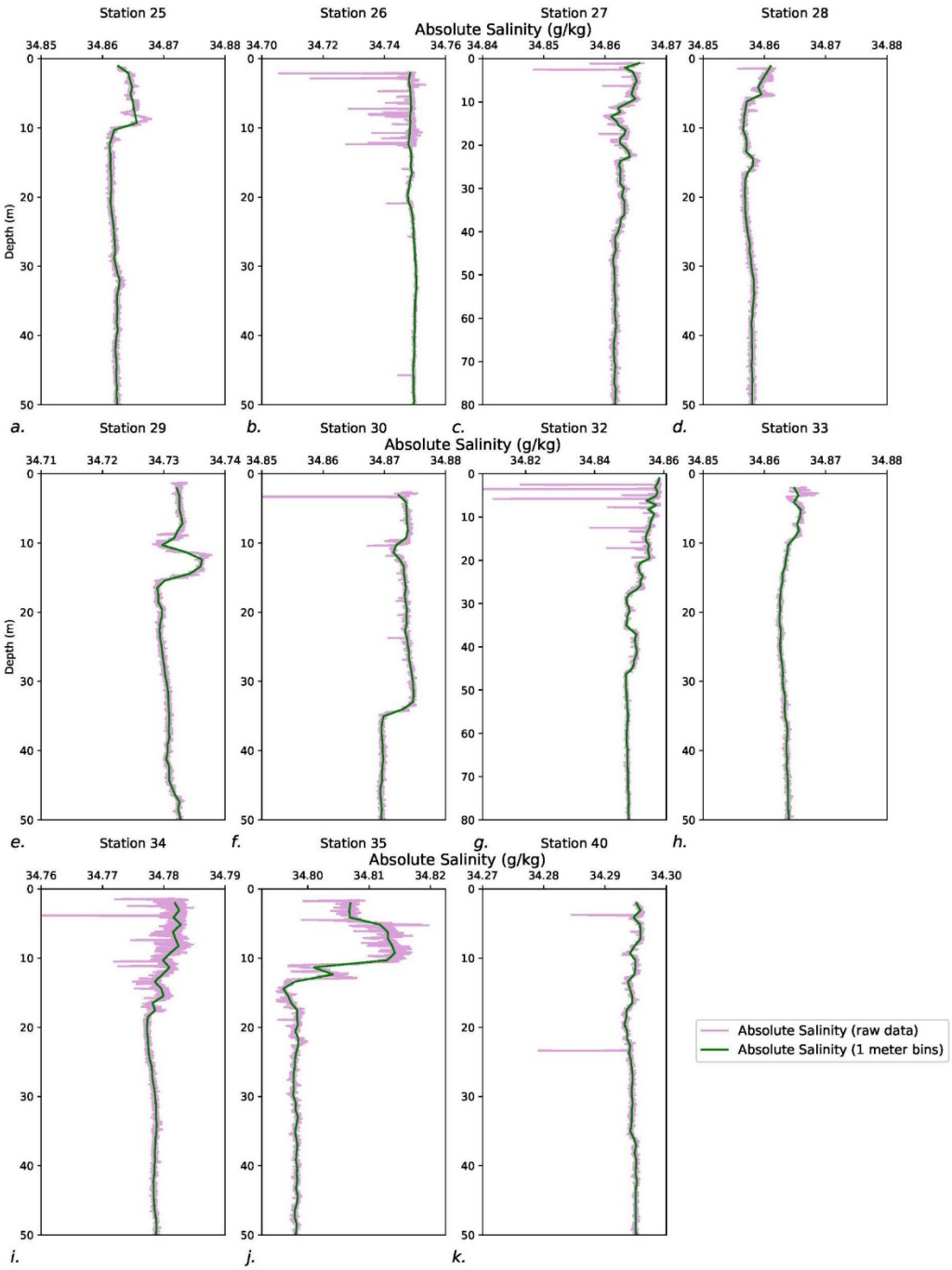

Supplemental Figure 1: Absolute Salinity plotted from raw conductivity data and from 1-meter binned data for the CTD Stations with anomalies. The x-axis for a, c, d-f, h-k are all 0.03 g kg^{-1}; b and g 0.06 g kg^{-1}. The raw data, plotted in purple, shows varying levels of noise in the signal and spikes of lesser magnitude values. This noise and the spikes in the data likely due to frazil ice crystal interference. Values of spikes extending off the plot: f: 34.670 g kg^{-1} ;g: 34.800g kg^{-1};i: 34.740g kg^{-1}. Plots b, c, i, j display more noise than the other plots. The 1-meter bin data, plotted in green, does not follow the spike excursions, indicating that binning the minimizes or removes the effects of the noise and spikes.

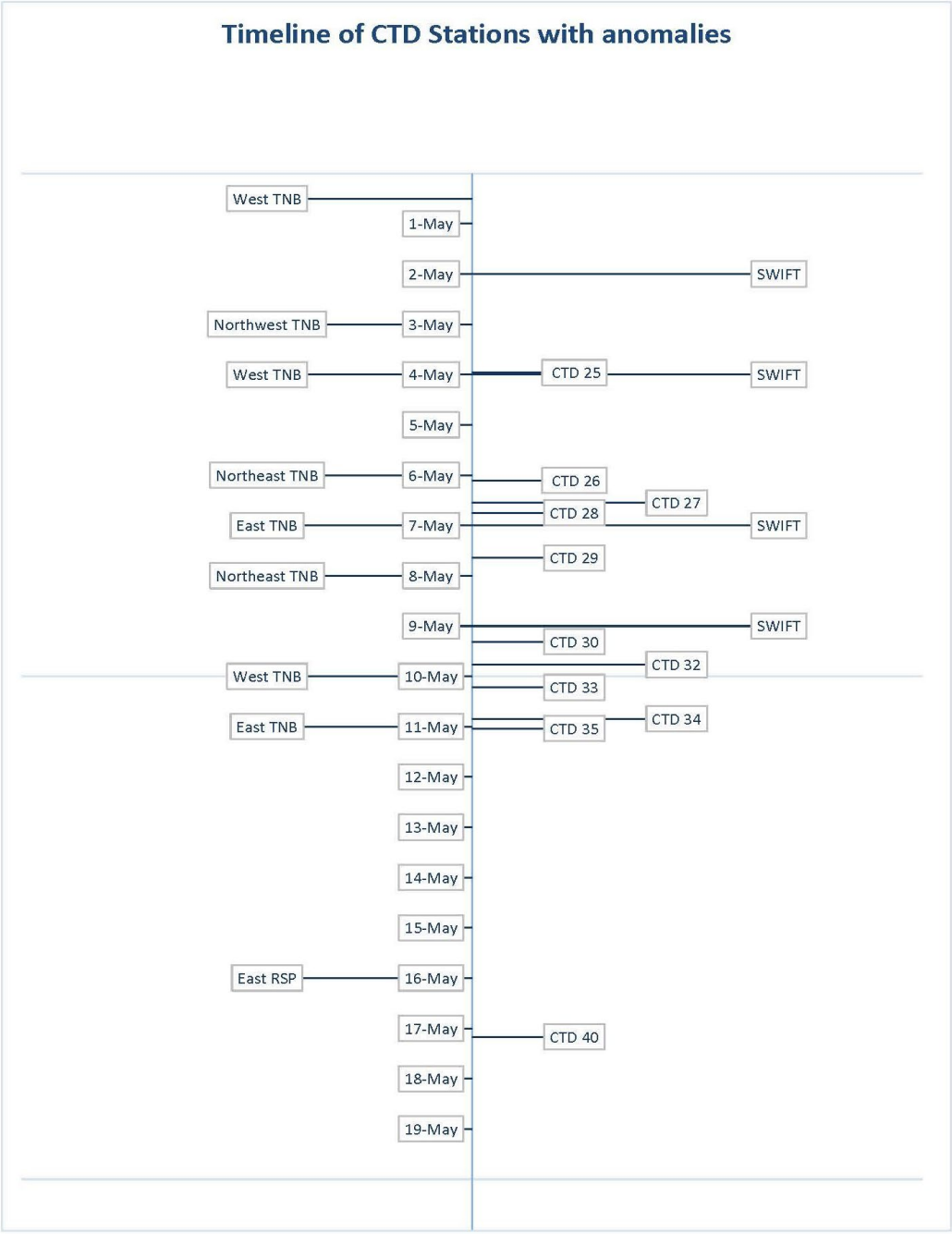

Supplemental Figure 2: Timeline of TNBP and RSP CTD casts and SWIFT deployments. A timeline of CTD and SWIFT deployments while in TNBP and RSP. To the left of the date, the geographic region is noted. This indicates when NB Palmer entered that portion of each polynya. The NB Palmer was in TNBP from May 1 to May 13. The NB Palmer was in the RSP from May 16 to May 18. To the right of the date the CTD stations with anomalies and SWIFT deployments are shown. All of the SWIFT deployments where in TNBP.

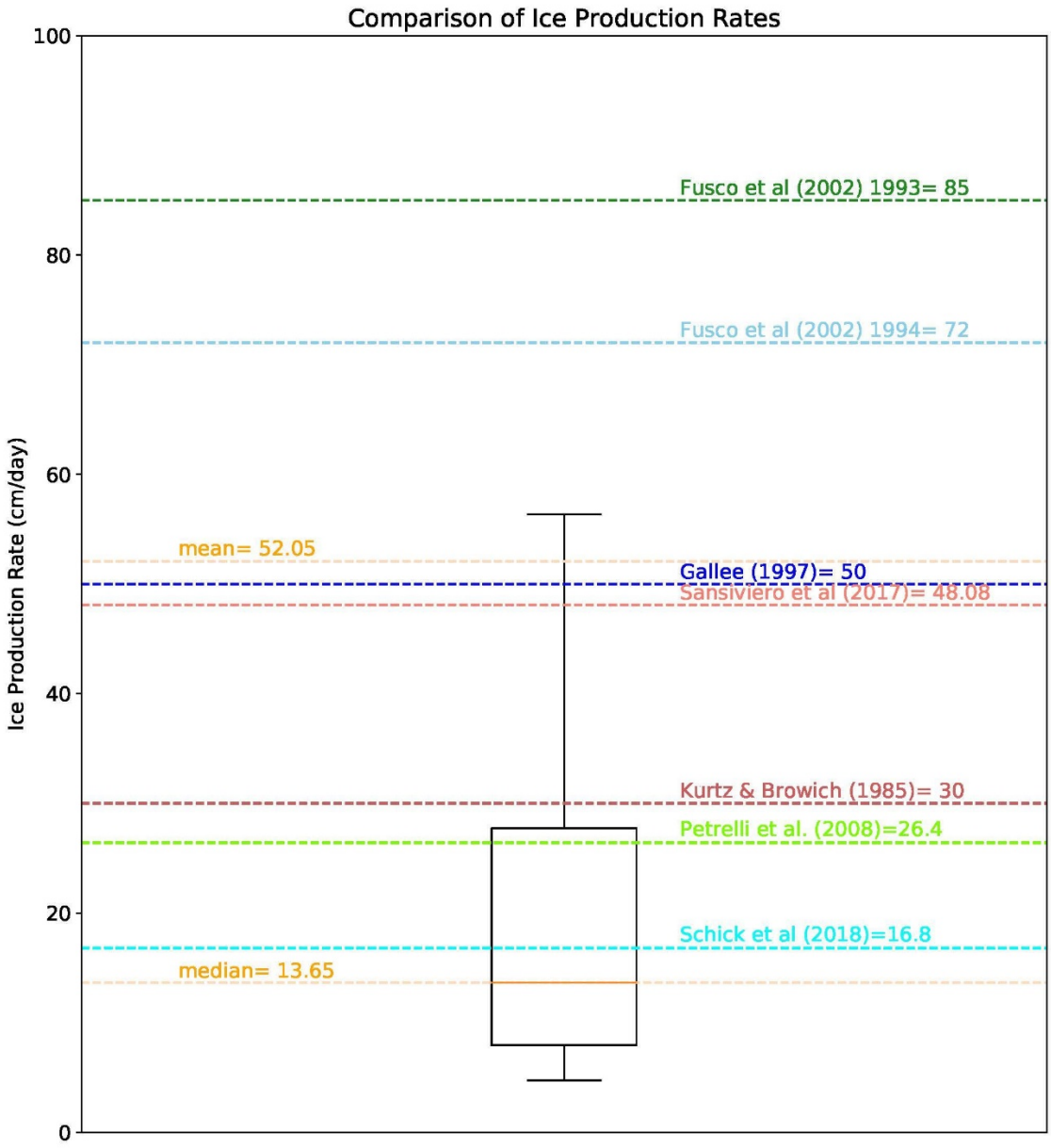

Supplemental Figure 3: Comparison of Ice production rates. This box and whisker plot shows the production rates calculated in this study. Station 35, marked as an outlier is not shown, but was included in the mean and median calculations.

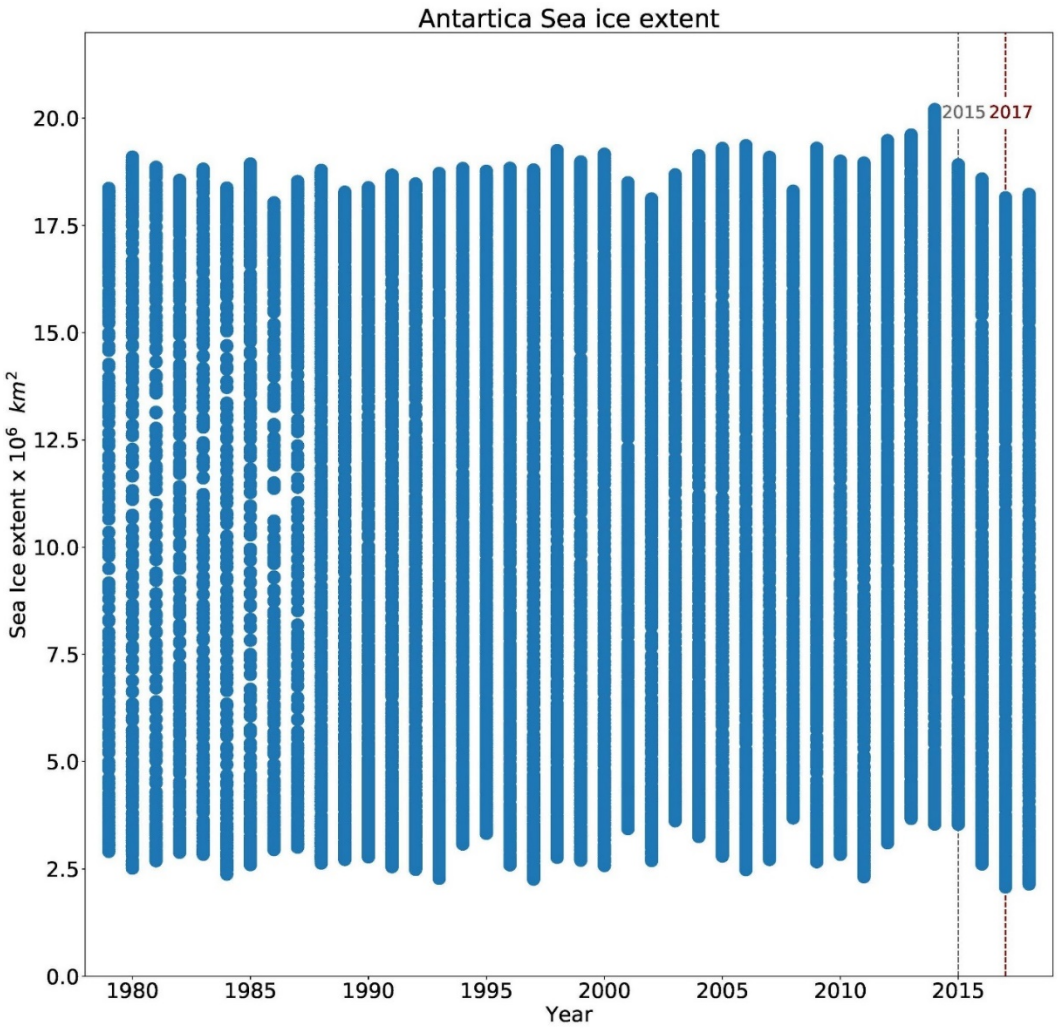

Supplemental Figure 4: Antarctic Sea ice extent. This plot shows the daily sea ice extent for Antarctica plotted over the entire year from 1978 to 2018. In 2015, the sea ice extent started to decline, with 2017 representing an unusually low sea ice extent.

BIBLIOGRAPHY

Armstrong, T. (1972). *World Meteorological Organization. WMO sea-ice nomenclature. Terminology, codes and illustrated glossary. Edition 1970. Geneva, Secretariat of the World Meteorological Organization, 1970, [ix], 147 p. [including 175 photos] + corrigenda slip. (WMO/OMM/BMO, No. 259, TP. 145.)*. *Journal of Glaciology - J GLACIOLOGY* (Vol. 11). https://doi.org/10.1017/S0022143000022577

Bromwich, D. H., & Kurtz, D. D. (1984). Katabatic wind forcing of the Terra Nova Bay polynya. *Journal of Geophysical Research*, *89*(C3), 3561. https://doi.org/10.1029/JC089iC03p03561

Buffoni, G., Cappelletti, A., & Picco, P. (2002). An investigation of thermohaline circulation in Terra Nova Bay polynya. *Antarctic Science, 14*(1), 83-92. doi:10.1017/S0954102002000615

Coachman, L. K. (1966), Production of supercooled water during sea ice formation, in *Proceedings of the Symposium on Arctic Heat Budget and Atmospheric Circulation*, pp. 497–529, RAND Corp., Santa Monica, Calif.

Comiso J.C. & Gordon A.L. (1998). Inter-annual variability in summer sea ice minimum, coastal polynyas and bottom water formation in the Weddell Sea. In M.O. Jeffries (ed): Antarctic sea ice: physical processes, interactions and variability. Pp. 293–315. Washington DC: American Geophysical Union.

Cox, G. F. N., & Weeks, W. F. (1983). Equations for determining the gas and brine volumes in sea-ice samples. *Journal of Glaciology* (Vol. 29). Retrieved from

https://www.igsoc.org/journal/29/102/igs_journal_vol29_issue102_pg306-316.pdf

Cushman-Rosin, B. (2019). *Environmental Fluid Mechanics*. New York: John Wiley & Sons.

Dmitrenko, I. A., Wegner, C., Kassens, H., Kirillov, S. A., Krumpen, T., Heinemann, G., … Busche, T. (2010). Observations of supercooling and frazil ice formation in the Laptev Sea coastal polynya. *Journal of Geophysical Research*, *115*(C5), C05015. https://doi.org/10.1029/2009JC005798

Fairall, C.W., E.F. Bradley, J.E. Hare, A.A. Grachev, and J.B. Edson (2003), Bulk parameterization of air sea fluxes: updates and verification for the COARE algorithm, J. Climate, 16, 571-590.

Fetterer, F., K. Knowles, W. N. Meier, M. Savoie, and A. K. Windnagel. 2017, updated daily. *Sea Ice Index, Version 3*. Sea Ice Index, Version 3. Boulder, Colorado USA. NSIDC: National Snow and Ice Data Center. doi: https://doi.org/10.7265/N5K072F8. 09 March 2019.

Fusco, G., Flocco, D., Budillon, G., Spezie, G., & Zambianchi, E. (2002). Dynamics and variability of Terra Nova Bay polynya. Marine Ecology, 23(SUPPL. 1), 201–209. https://doi.org/10.1111/j.1439-0485.2002.tb00019.x

Fusco, Budillon, & Spezie. (2009). Surface heat fluxes and thermohaline variability in the Ross Sea and in Terra Nova Bay polynya. Continental Shelf Research, 29(15), 1887-1895.

Gallée, H. (1997). Air-sea interactions over Terra Nova Bay during winter: Simulation with a coupled atmosphere-polynya model. *Journal of Geophysical Research: Atmospheres*, *102*(D12), 13835–13849. https://doi.org/10.1029/96JD03098

Heorton, H. D. B. S., & Feltham, D. L. (n.d.). A Model of Sea Ice Formation in Leads and Polynyas. https://doi.org/10.1175/JPO-D-16-0224.1

Ito, M., Ohshima, K. I., Fukamachi, Y., Simizu, D., Iwamoto, K., Matsumura, Y., … Eicken, H. (2017). Observations of supercooled water and frazil ice formation in an Arctic coastal polynya from moorings and satellite imagery. https://doi.org/10.3189/2015AoG69A839

Jacobs, S. (2004). Bottom water production and its links with the thermohaline circulation. *Antarctic Science, 16*(4), 427-437. doi:10.1017/S095410200400224X

Jenkins, A., & Bombosch, A. (1995). Modeling the effects of frazil ice crystals on the dynamics and thermodynamics of Ice Shelf Water plumes. *Journal of Geophysical Research*, *100*(C4), 6967. https://doi.org/10.1029/94JC03227

Jones, D. W. R., & Wells, A. J. (2018). Frazil-ice growth rate and dynamics in mixed layers and sub-ice-shelf plumes. *The Cryosphere*, *12*, 25–38. https://doi.org/10.5194/tc-12-25-2018

Kurtz, D. D., & Bromwich, D. H. (1985). A Recurring, Atmospherically forced polynya in terra nova bay. Oceanology of the Amarcric Cominenral Shelf Antarctic Research Series (Vol. 43).

Li, N., Kinzelbach, W., Li, W., & Dong, X. (2015). Box model and 1D longitudinal model of flow and transport in Bosten Lake, China. *Journal of Hydrology*, *524*, 62–71. https://doi.org/10.1016/J.JHYDROL.2015.02.032

Lombardo, C., & Gregg, M. (1989). Similarity scaling of viscous and thermal dissipation in a convecting surface boundary layer. *Journal of Geophysical Research, 94*(C5), 6273-6284.

Mathiot, P., Jourdain, N., Barnier, C., Gallée, B., Molines, H., Sommer, J., & Penduff, M. (2012). Sensitivity of coastal polynyas and high-salinity shelf water production in the Ross Sea, Antarctica, to the atmospheric forcing. Ocean Dynamics, 62(5), 701-723.

Manwell, J. F., McGowan, J. G., & Rogers, A. L. (2010). Wind Energy Explained: Theory, Design and Application.

Manzella, G. M. R., R. Meloni, and P. Picco, Current, temperature and salinity observations in the Terra Nova Bay polynya area, in Oceanography of the Ross Sea, edited by G. Spezie and G. M. R. Manzella, pp 165-173, Springer-Verlag, New York, 1999.

Martin, S., Drucker, R. S., & Kwok, R. (2007). The areas and ice production of the western and central Ross Sea polynyas, 1992-2002, and their relation to the B-15 and C-19 iceberg events of 2000 and 2002. *Journal of Marine Systems.* https://doi.org/10.1016/j.jmarsys.2006.11.008

Matsumura, Y., & Ohshima, K. I. (2015). Lagrangian modelling of frazil ice in the ocean. *Annals of Glaciology*, *56*(69), 373–382. https://doi.org/10.3189/2015AoG69A657

Michel, B. (1967). Physics of Snow and Ice: Morphology of Frazil Ice (Vol. 1, pp. 119–128).

Monin, A. S., & Obukhov, A. M. (1954). Basic laws of turbulent mixing in the surface layer of the atmosphere. *Contrib. Geophys. Inst. Acad. Sci. USSR*, *151*(163), e187.

Morales Maqueda, M. A., Willmott, A. J., & Biggs, N. R. T. (2004). Polynya Dynamics: a Review of Observations and Modeling. *Reviews of Geophysics*, *42*(1), RG1004. https://doi.org/10.1029/2002RG000116

Orsi, & Wiederwohl. (2009). A recount of Ross Sea waters. Deep-Sea Research Part II, 56(13), 778-795.

Overland, J. E. (1985). Atmospheric boundary layer structure and drag coefficients over sea ice. Journal of Geophysical Research, 90(C5), 9029–9049. https://doi.org/10.1029/JC090iC05p09029

Park, J., Kim, H.-C., Jo, Y.-H., Kidwell, A., & Hwang, J. (2018). Multi-temporal variation of the Ross Sea Polynya in response to climate forcings. *Polar Research*, *37*(1), 1444891. https://doi.org/10.1080/17518369.2018.1444891

Pease, C. H. (1987). The size of wind-driven coastal polynyas. *Journal of Geophysical Research*, *92*(C7), 7049. https://doi.org/10.1029/JC092iC07p07049

Petrelli, P., Bindoff, N.L., Bergamasco, A., 2008. The sea ice dynamics of Terra Nova Bay and Ross Ice Shelf Polynyas during a spring and winter simulation. J. Geophys. Res.

Roberts, P. J., & Webster, D. R. (2002). *Turbulent diffusion*(pp. 7-47). ASCE Press, Reston, Virginia.

Sansiviero, M., Morales Maqueda, M. Á., Fusco, G., Aulicino, G., Flocco, D., & Budillon, G. (2017). Modelling sea ice formation in the Terra Nova Bay polynya. *Journal of Marine Systems*, *166*, 4–25. https://doi.org/10.1016/J.JMARSYS.2016.06.013

SBE 911plus CTD | Sea-Bird Scientific USA - Downloads | Hach. (n.d.). Retrieved August 15, 2018, from https://www.seabird.com/profiling/sbe-911plus-ctd/family-downloads?productCategoryId=54627473769

Skogseth, R., Nilsen, F., & Smedsrud, L. H. (2009). Supercooled water in an Arctic polynya: observations and modeling. Journal of Glaciology, 55(189), 43–52. https://doi.org/10.3189/002214309788608840

Talley, L.D., Picard, G.L., Emery, W.J. Swift, J.H. *Physical Properties of Seawater 3.1. Molecular properties of water*. (2011).

Tamura, T., Ohshima, K. I., & Nihashi, S. (2008). Mapping of sea ice production for Antarctic coastal polynyas. Geophysical Research Letters, 35(7), 1–5. https://doi.org/10.1029/2007GL032903

Thomson, J. (2012). Wave breaking dissipation observed with “swift” drifters. Journal of Atmospheric and Oceanic Technology, 29(12), 1866–1882. https://doi.org/10.1175/JTECH-D-12-00018.1

Thomson, J. (2012). Wave breaking dissipation observed with “swift” drifters. Journal of Atmospheric and Oceanic Technology, 29(12), 1866–1882. https://doi.org/10.1175/JTECH-D-12-00018.1

Tsang, G., O ', T., & Hanley, D. (1985). Frazil formation in water of different salinities and supercoolings. *Journal Of Glaciology*, *31*(108).

Ushio S., & Wakatsuchi, M. (1993). a Laboratory Study on Supercooling and Frazil Ice Production Processes in Winter Coastal Polynyas. *Journal Of Geophysical Research-Oceans*, *98*(C11), 20321–20328. https://doi.org/10.1029/93JC01905

Van Woert, M. L., The wintertime expansion and contraction of the Terra Nova Bay polynya, in Oceanography of the Ross Sea: Antarctica, edited by G. Spezie and G. M. R. Manzella, pp. 145-164, Springer-Verlag, New York, 1999a

Van Woert, M. L., Wintertime dynamics of the Terra Nova Bay polynya, J. Geophys. Res., 104, 7753-7769, 1999b.

Wakatsuchi, M., & Ono, N. (1983). Measurements of salinity and volume of brine excluded from growing sea ice. *Journal of Geophysical Research*, *88*(C5), 2943. https://doi.org/10.1029/JC088iC05p02943

Wilchinsky, A. V., Heorton, H. D. B. S., Feltham, D. L., Holland, P. R., Wilchinsky, A. V., Heorton, H. D. B. S., … Holland, P. R. (2015). Study of the Impact of Ice Formation in Leads upon the Sea Ice Pack Mass Balance Using a New Frazil and Grease Ice Parameterization. *Journal of Physical Oceanography*, *45*(8), 2025–2047. https://doi.org/10.1175/JPO-D-14-0184.1